Subcellular mRNA localization patterns across tissues resolved with spatial transcriptomics

Roy Novoselsky[1], Ofra Golani[2], Tal Barkai[1,3], Merav Kedmi[2], Inna Goliand[2], Michal Fine[1], Ilan Kent[4,5], Ido Nachmany[4,5], Shalev Itzkovitz[1*].

[*]Equal contribution

[1]Department of Molecular Cell Biology, Weizmann Institute of Science, Rehovot, Israel.

[2]Department of Life Sciences Core Facilities, Weizmann Institute of Science, Rehovot, Israel.

[3]Sheba Medical Center, Ramat Gan, Israel.

[4]Faculty of Medicine and Health Sciences, Tel Aviv University, Tel Aviv, Israel.

[5]Department of General Surgery and Transplantation, Sheba Medical Center, Ramat Gan, Israel.

These authors contributed equally: Roy Novoselsky, Ofra Golani

* Corresponding author: shalev.itzkovitz@weizmann.ac.il

Abstract

Subcellular RNA localization, including nuclear retention and apical-basal compartmentalization in polarized epithelia plays a central role in post-transcriptional regulation. However, methods for high-throughput mapping of mRNA localization within intact tissue sections remain limited. Here, we apply high-resolution spatial transcriptomics (VisiumHD) to systematically resolve intracellular mRNA localization across diverse mammalian tissues. We introduce a computational approach that extracts subcellular features from spatial data and quantifies transcript localization patterns. Using this framework, we map apical-basal mRNA localization and nuclear retention in gastrointestinal epithelia and in liver hepatocytes. Our analyses reveal conserved and tissue-specific localization signatures that can be readily obtained from standard high-definition spatial transcriptomics experiments. This approach broadens the scope of spatial transcriptomics by enabling routine investigation of intracellular RNA distributions in both healthy and diseased tissues.

Introduction

Spatial transcriptomics has revolutionized our ability to study gene expression within intact tissue environments, preserving both tissue architecture and cellular neighborhoods. However, most applications to date have focused on intercellular variation, with limited investigation of mRNA organization at the subcellular level. Understanding how transcripts are spatially distributed within cells offers unique insights into post-transcriptional regulation and functional cell polarity. This is supported by growing evidence that intracellular mRNA localization plays a critical role in mammalian cell biology (1–11). One well-characterized form of mRNA localization is apical-basal compartmentalization in epithelial cells, where specific transcripts are preferentially enriched in either the apical or basal domain(12–16). Another form of mRNA localization is nuclear retention, which is traditionally associated with splicing-defective or non-coding RNAs, but has also been observed for fully spliced transcripts in mammalian cells (17–20).

Previously, high-throughput mapping of mRNA localization within tissues has been time-consuming and technically demanding. Early approaches relied primarily on labor-intensive methods such as fractionation-based sequencing and laser capture microdissection (LCM). Recent technological advances have expanded the toolkit for studying spatial RNA localization, utilizing either targeted imaging-based techniques such as Xenium (21), MERSCOPE (22), CosMx (23) and seqFISH (24), or spatial sequencing-based spatial transcriptomics approaches, such as VisiumHD (25), StereoSeq (26) and SlideSeq (27). Computational tools modeling data from imaging-based techniques yielded important insights into subcellular mRNA localization (28–30). However, similar tools to extract sub-cellular localization information from spatial sequencing techniques are currently lacking. Here, we develop HiVis, a user-friendly framework for spatial transcriptomics that combines advanced image-processing approaches to enable subcellular mRNA localization analyses. We systematically profile apical-basal mRNA polarization and nuclear retention across multiple mouse and human tissues using VisiumHD and demonstrate that our computational tool resolves subcellular transcript distribution and identifies polarized and nuclear-retained mRNAs in organs such as the small intestine, colon, and liver.

Results

Development of computational platform for VisiumHD analysis

Mapping subcellular mRNA localization across tissues requires an integrated approach that combines high-resolution image analysis with a flexible computational framework for downstream transcriptomic analysis. While tools such as *bin2cell* (31), *SpatialData* (32), Enact (33) and *Thor* (34) provide powerful frameworks at the cell or tissue scale, they do not facilitate a streamlined analysis of RNA subcellular localization.

To address this gap, we developed HiVis (HD Integrated Visium Interactive Suite), an interactive, user-friendly, end-to-end platform optimized for 10x VisiumHD datasets but extended to support other spatial transcriptomics methods (Fig. S1). HiVis enables robust identification of subcellular compartments and supports application across a wide range of tissues and experimental conditions. The main features of the tool are:

- Integration with QuPath (35), providing a powerful image analysis toolkit that includes pixel classification, interactive annotation, and object feature extraction.
- Flexible, tissue-oriented segmentation and aggregation, supporting multiple levels of resolution (e.g., bins, single cells, or other objects) with algorithms such as StarDist (36), Cellpose (37), and InstanSeg (38).
- Bidirectional data transfer between bins and cells (or other objects), enabling aggregation from bin to cell level as well as redistribution of cell-level information back to bins. This allows both global cell-level analysis and fine-grained subcellular investigation.
- Comprehensive downstream analysis and visualization, with full compatibility with widely used spatial transcriptomics frameworks such as Scanpy (39) and Squidpy (40).

We applied HiVis to systematically assess mRNA localization across multiple tissues. To this end, we analyzed both published and publicly available datasets, as well as newly generated VisiumHD data from livers of two mice. Using this framework, we mapped apical-basal localization patterns in mouse small intestine, human colon, and the more complex architecture of mouse liver (Fig. 1). In addition, we profiled nuclear-cytoplasmic localization in these tissues, as well as in human liver. We validated our results using LCM and fractionated RNA sequencing (RNA-seq) datasets. To further validate our findings, we performed single-molecule fluorescence in situ hybridization (smFISH) or hybridization chain reaction (HCR-FISH).

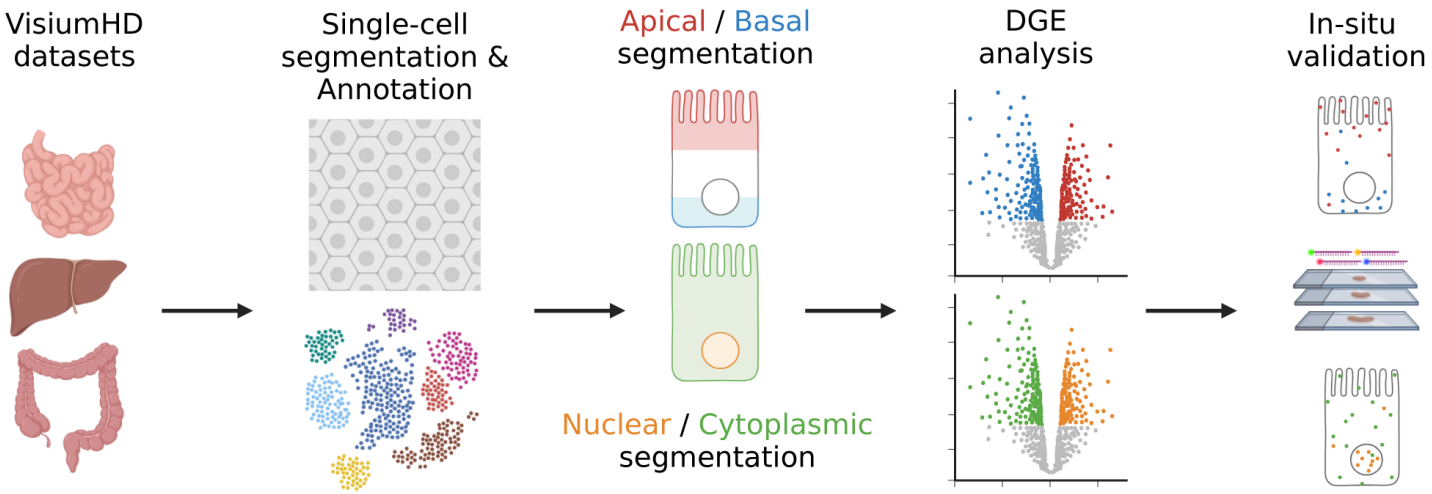

Figure 1 – Workflow for detection of subcellular mRNA localization using HiVis

Analysis workflow for VisiumHD datasets. Images are segmented into single cells, tissue and cell type specific information is incorporated to enable precise subcellular analyses. Apical–basal and nuclear–cytoplasmic compartments are assigned to spatial bins, and differential gene expression analysis is performed to identify genes localized to these compartments. Validation is carried out using in-situ hybridization stainings. The diagram was created with BioRender.com.

Reconstructing zonation patterns in mouse small intestine and liver using HiVis

Epithelial tissues such as the intestine and the liver exhibit pronounced zonation patterns, which strongly influence gene expression and cellular function (41–44). Delineating cell states across these spatial domains is therefore not only a critical first step in tissue-level analysis, but also an essential prerequisite for interpreting subcellular RNA localization.

To assess our ability to reconstruct zonation patterns using HiVis, we analyzed a publicly available VisiumHD dataset of the mouse small intestine (10x genomics, 2024). Because many villi were damaged in the tissue handling process (i.e. Swiss-roll preparation), and to minimize bias from proximal–distal variation (45), we restricted our analysis to the proximal small intestinal segment (Fig. S2a), which contained intact crypt-villi units. We performed single-cell segmentation (Fig. 2a) followed by aggregation of all 2×2 µm bins included in each cell, to obtain single-cell resolved data. This enabled transcriptomic analysis and cell-type assignment using standard single cell RNA-seq (scRNA-seq) workflows (Fig. 2b–d, S2b–e). The identified cell types were consistent with their expected spatial organization along the intestinal epithelium (e.g., muscle, Paneth cells, and enterocyte zones from villus base to tip).

To establish spatial zonation independently of the transcriptome, we manually segmented individual villi (Fig. S2f) and identified the muscle layer using a pixel classifier (Fig. S2g). Based on this annotation, we calculated the distance of each bin and cell from the muscle layer (Fig. S2h–i). Restricting the analysis to epithelial cells, we then compared gene expression patterns between cells at the villi tips and bases (Fig. 2e, Supplementary table 1). The resulting zonation profiles showed strong concordance with previously published scRNA-seq data that was focused on zonation patterns across the villus axis (41), with a correlation of r=0.87 (Fig. 2f). This confirms that HiVis can accurately reconstruct villus zonation, establishing the spatial framework required for subsequent subcellular localization analyses.

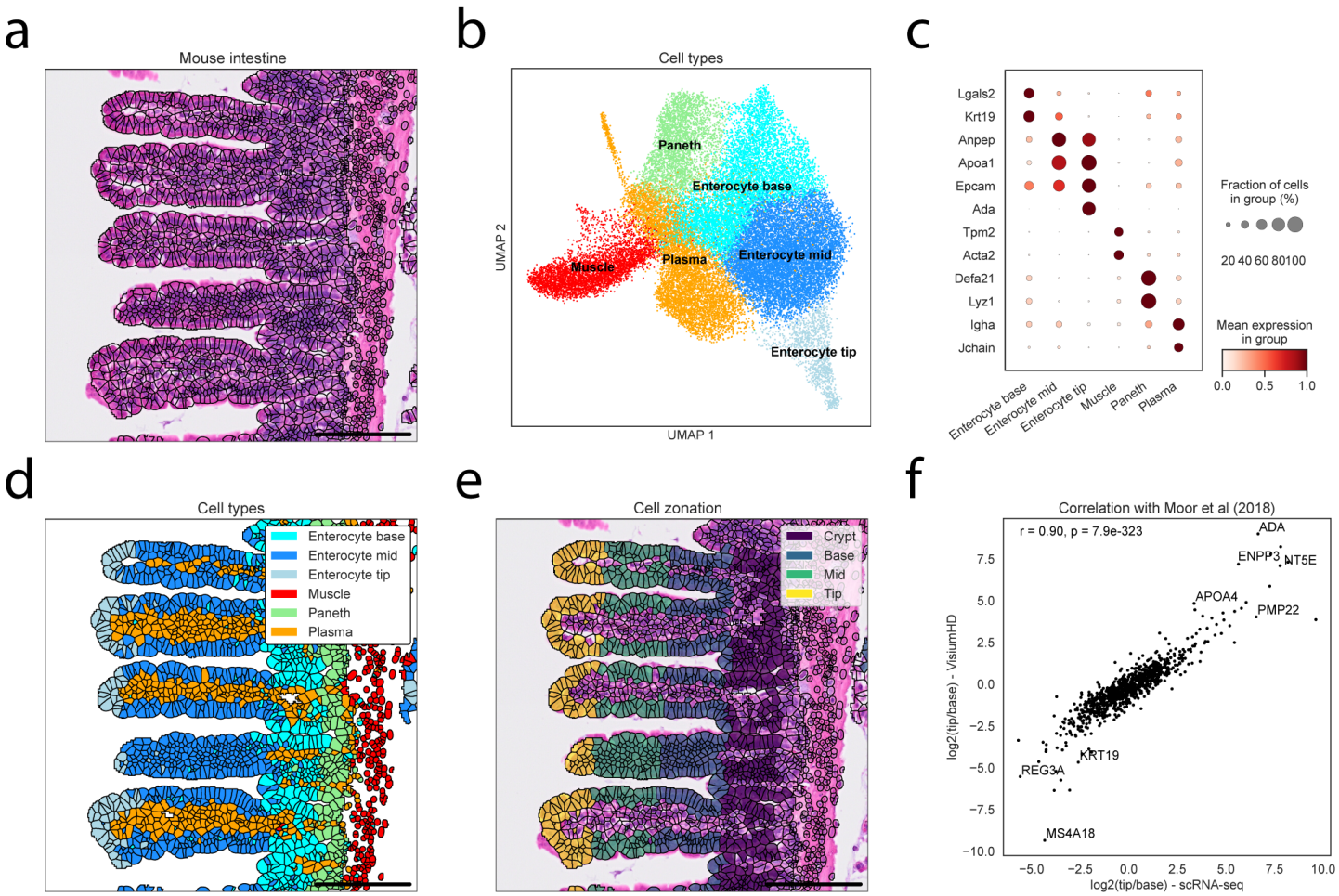

Figure 2 – Reconstructing zonation along the crypt-villus axis in the mouse small intestine

(a) Single-cell segmentation of mouse small intestine VisiumHD. Scale bar 100 µm. **(b)** UMAP of single cells colored by cell type. **(c)** Dot plot of normalized gene expression for selected markers across cell types. **(d)** Same field of view (FOV) as (a), with cells colored by cell type. Colors correspond to the cluster colors in (b)**.** **(e)** Same FOV as (a), with cells colored by villus zones. **(f)** Spearman correlation of center of mass (COM, Methods) between the current VisiumHD analysis and previously published scRNA-seq data (41). Selected gene names are shown.

Next, we generated VisiumHD data from livers of two mice. We stained the sections with DAPI, which stains nuclei, and fluorescently-labeled antibodies against Na^+/K^+-ATPase (ATP1A1) and CD31 to facilitate identification of nuclear, membrane and basal (sinusoidal-facing) cellular compartments respectively (Fig. 3a-b, S3a). Using HiVis, we segmented hepatocytes (parenchymal cells) and non-parenchymal cells (NPC) independently, based on regions depicted by a pixel classifier (Fig. 3b, S3b, Methods). We then aggregated the included 2×2 µm bins to obtain single cell transcriptomics, and reconstructed hepatocytes zonation maps based on established landmark genes (Fig. 3c, S3c, Methods), as previously described (46). From this, we derived zonation profiles for each gene, which were highly consistent across the two samples (Fig. S3d, Supplementary table 1). These profiles showed strong positive correlations with previously published zonation profiles that were based on either spatially-resolved scRNA-seq (43) or high-definition spatial transcriptomics data obtained using Stereo-seq (47) (Fig. 3d).

As our single-cell segmentation was based on membrane-staining, we could use morphological features extracted from the single-cell segmentation. We found that as previously shown (48), the overall sizes of hepatocytes decreased significantly from the central vein towards the portal vein (r=-0.26, p<1e-300, Fig.

S3e). Hepatocytes in mice contain either one or two nuclei, with distinct ploidy levels that scale with nuclear size (49). Using the number of nuclei and their sizes, we assigned a ploidy class for each cell (Fig. S3f). In concordance with previously published results (49) we found that hepatocytes in the mid-lobule zones in mice exhibited higher ploidy compared to central and portal hepatocytes (Fig. 3e). These results demonstrate that HiVis can accurately reconstruct lobular zonation in the liver. We next turned to investigate subcellular RNA localization in zonally stratified cells in these two stereotypically zonated tissues.

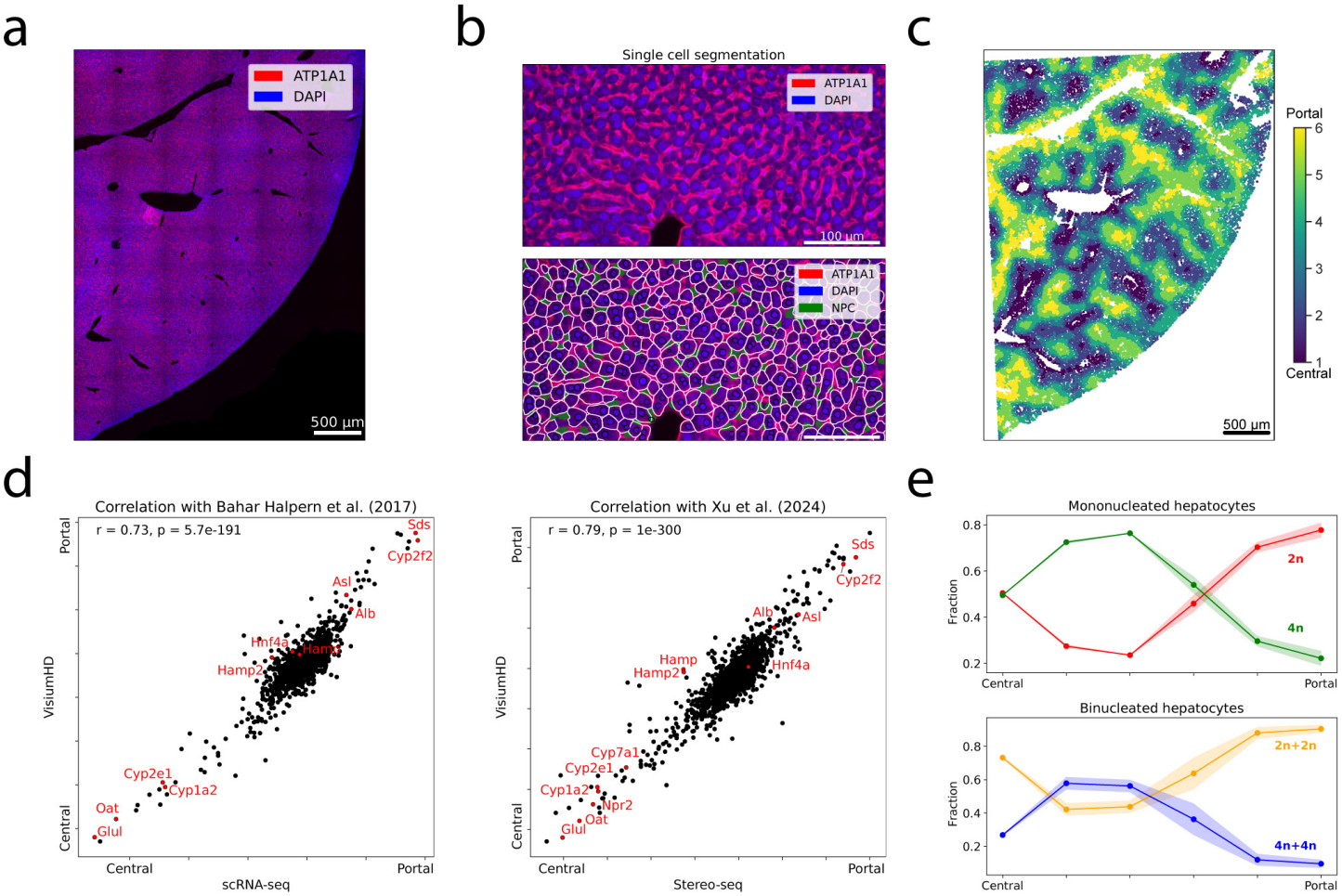

Figure 3 – Reconstructing hepatocyte zonation across liver lobules

(a) VisiumHD immunofluorescence image of mouse liver. Representative image of 2 samples. **(b)** Mouse liver VisiumHD immunofluorescence image (top) and overlayed with single-cell segmentation (bottom). NPC – non parenchymal cells, residing in the sinusoids, which are segmented based on CD31 and ATP1A1 staining (Methods). **(c)** Single-cell VisiumHD data of mouse liver, colored by zones along the central-portal axis. Shown is a representative plot from one mouse. **(d)** Spearman correlation plots of center of mass across liver zones based on current VisiumHD and previously published scRNA-seq (50) (left) and Stereo-seq spatial transcriptomics (47) (right). **(e)** Mean fraction of ploidy classes in both mononucleated (top) and binucleated (bottom) hepatocytes across the liver lobule in both mice. Patch is standard error of the mean.

Polarized mRNA distribution in the intestinal epithelium

Following the cell-level analysis of epithelial cells in the mouse intestine, we next investigated the subcellular distributions of mRNAs. The intestinal epithelium is composed of an apical side facing the nutrient and microbial enriched lumen, and a basal side facing the blood stream. These sides differ in morphology (51,52), protein (13,53) and even RNA content (13,14,16). To this end, we assigned apical and basal identities to 2×2 µm bins using a pixel classifier (Fig. 4a). Differential gene expression (DGE) analysis revealed transcripts significantly enriched in either the apical or basal domains (Fig. 4b, Supplementary table 2). The apical-basal enrichment patterns obtained with pixel classifier were consistent with those derived from manual annotations (r=0.83, p=6e-85, Fig S4a). We validated the apical polarization of Apob and the basal polarization of Net1 using smFISH (Fig. 4c). The resulting polarization profiles showed strong concordance with previously published data obtained by LCM of apical and basal compartments (14) (Fig. 4d). We next examined whether apical-basal polarization varies along the villus axis and found that profiles at the tip and base were largely similar, consistent with previous observations (14) (Fig. S4b). We further examined whether apically localized transcripts exhibit preferential luminal versus perinuclear enrichment (Fig. S4c–d) and observed clear differences between these patterns (Supplementary Table 2). For example, *Lct* showed strong luminal apical localization, whereas *Atp1b1* displayed a more uniformly distributed apical pattern (Fig. S4e–g).

These results demonstrated that our approach can accurately capture apical-basal polarization in intestinal epithelial cells, prompting us to extend the analysis to human colon tissue, a tissue in which epithelial mRNA polarization has not been systematically explored. To this end, we analyzed published VisiumHD data from five patients with colorectal cancer (25), focusing on adjacent normal or control regions. As in the small intestine, we classified bins into apical and basal epithelial compartments and performed DGE analysis (Fig. S4c) and identified transcripts enriched in each domain (Fig. 4e, Supplementary table 2). Correlation analysis of polarization profiles between colon and previously published jejunum data revealed highly similar patterns across the two organs (Fig. S4d). Apical transcripts included *PIGR*, *CDH1*, and *CES2*, whereas basal transcripts included *KTN1*, *NET1*, and *MYH14*. We validated *MYH14* and *PIGR* by HCR-FISH (Fig. 4f). Together, these results demonstrate that colon epithelial cells exhibit clear apical–basal mRNA polarization, extending this localization pattern to an additional segment of the gastrointestinal tract.

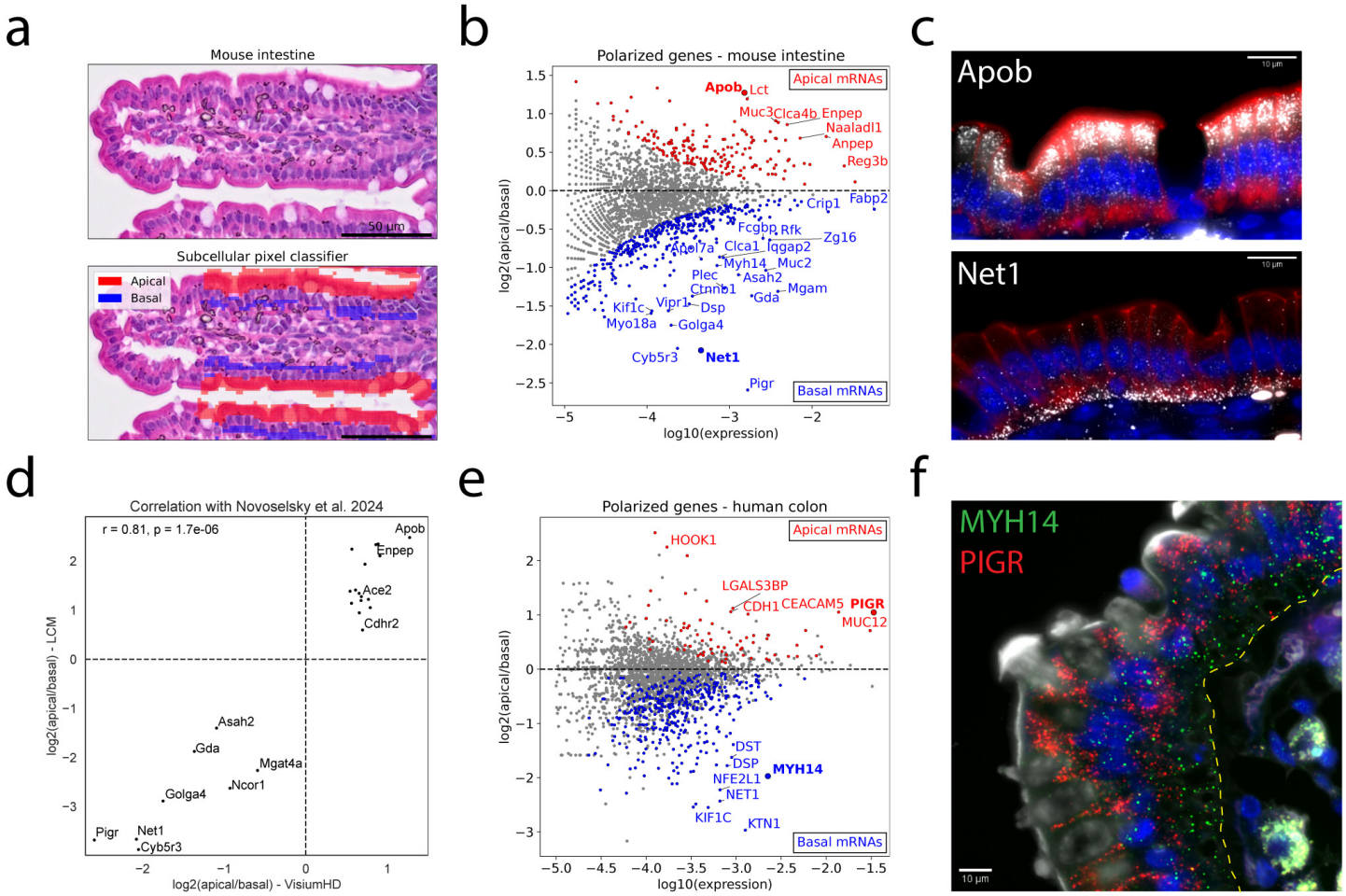

Figure 4 – Mapping apical-basal mRNA localization in mouse small intestine and human colon

(a) Mouse small intestine VisiumHD H&E image (top) and overlayed with 2×2µm bins colored by apical/basal assignment, based on a pixel classifier (bottom). **(b)** MA-plot of differential gene expression results in mouse proximal small intestine. Significant genes (q<0.05) are colored red and blue, bold genes shown in smFISH validation in (c). Selected gene names are shown. **(c)** smFISH staining of Apob (top) and Net1 (bottom) in mouse proximal small intestine. Red staining is E-cadherin which stains epithelial basolateral membranes, blue staining is DAPI. Scale bar, 10 µm. **(d)** Spearman correlation of apical/basal bias based on current VisiumHD and previously published scRNA-seq (14). Only genes with q<0.25 in both datasets are shown. **(e)** MA-plot of differential gene expression in human colon. Significant genes (q<0.25) are colored red and blue, bold genes shown in HCR-FISH validation in (f). Selected gene names are shown. **(f)** HCR-FISH staining of PIGR and MYH14 in human colon. White staining is Wheat Germ Agglutinin (WGA), blue staining is DAPI. Dashed yellow line marks the basal side of the epithelial cells, depicted by WGA staining. Images in (c) and (f) are representative of 2 individuals. Scale bar, 10 µm.

Specific mRNAs are basally localized in mouse hepatocytes

Having demonstrated that HiVis can resolve apical-basal transcript localization in the simple columnar epithelium of the digestive tract, we next turned to a more complex tissue: the mouse liver. Hepatocytes in the mammalian liver are arranged in radial sheets that span the portal-central axis. Each hepatocyte has two basal sides, facing the sinusoidal blood vessels, and cortical sides that face adjacent hepatocytes (these include the apical sides that face the bile canaliculi) (54). In this case, apical and basal domains are not easily identifiable and therefore cannot be reliably isolated by LCM. As a result, mRNA localization to these compartments has remained uncharacterized, making it an ideal test case for our approach. Our VisiumHD data included staining for ATP1A1 and CD31, which marked membranes and sinusoidal endothelial cells respectively. Using these markers, we identified sinusoids between hepatocytes (Fig. 5a) and calculated the distance of each bin within hepatocytes to both the nearest sinusoid and to the cell border (Fig. 5b). This enabled assignment of cortical (close to any membrane regardless of distance from sinusoids) and basal (close to sinusoids) identities to each bin (Fig. 5c–d). Differential gene expression analysis identified several basally enriched transcripts, including *Scd1*, *Pigr*, *Cald1*, and *Cyb5r3* (Fig. 5e, Supplementary table 2). Validation by smFISH confirmed basal localization of *Pigr* and *Cyb5r3* (Fig. 5f), providing, to our knowledge, the first evidence of cytoplasmic mRNA polarization in hepatocytes. These findings demonstrate that HiVis can be applied to VisiumHD data from complex tissues to resolve subcellular mRNA localization.

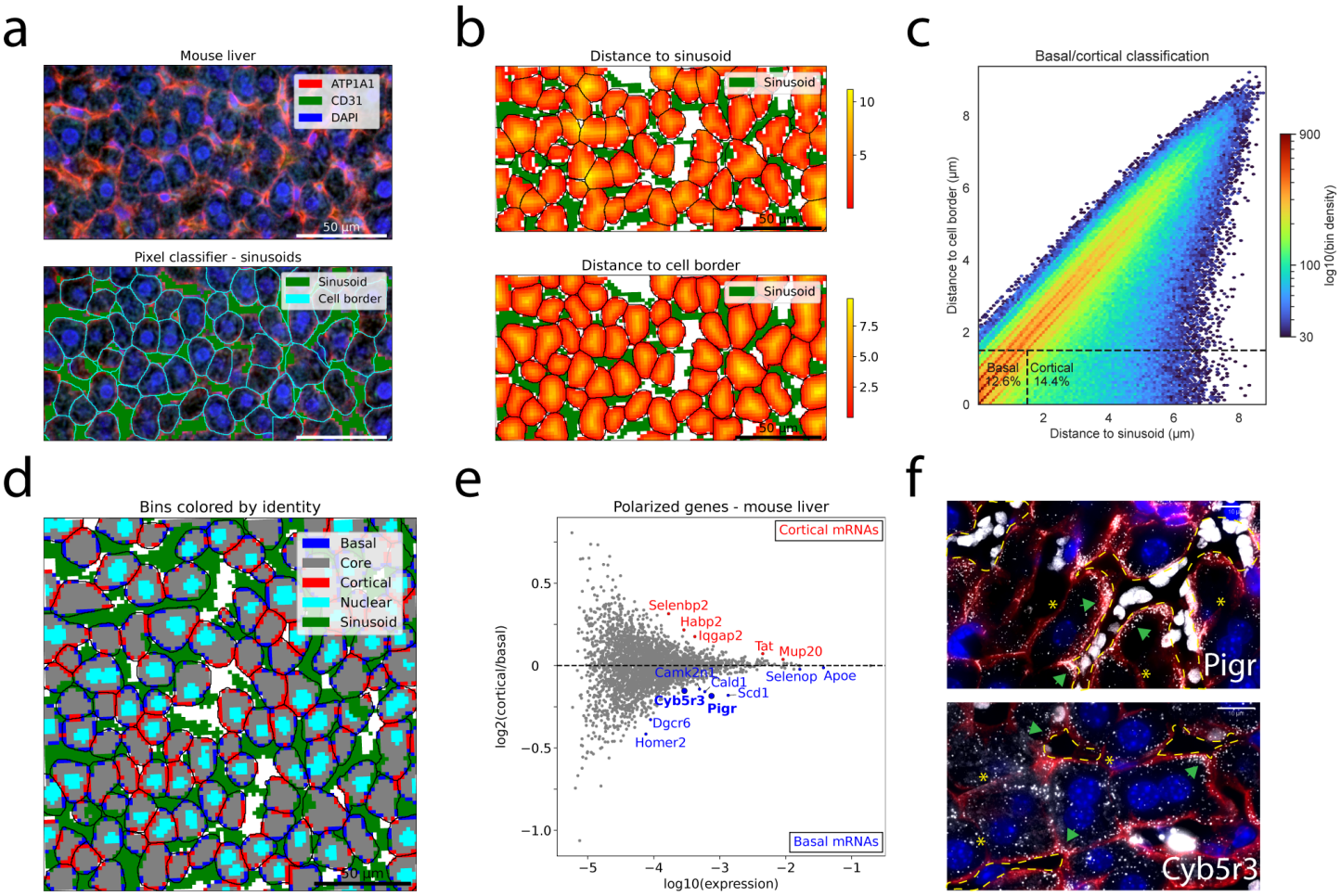

Figure 5 – Mapping basal mRNA localization in mouse liver

(a) Mouse liver VisiumHD immunofluorescence image (top) and overlayed with 2×2μm sinusoid bins, based on a pixel classifier and with cells segmentation (bottom). **(b)** Same FOV as (a), with bins colored by distance to sinusoids (top) and distance to cell border (bottom). Distance is in μm. **(c)** Representative density plot of 2×2μm bins from one mouse liver. Black squares indicate the bins that were classified as cortical or basal. **(d)** 2×2μm bins in mouse liver, colored by intracellular location. **(e)** MA-plot of differential gene expression in mouse liver. Significant genes (q<0.25) are colored red, blue genes are shown in smFISH validation in (f). Selected gene names are shown. **(f)** smFISH staining of Pigr (top) and Cyb5r3 (bottom) in mouse liver. Red staining is ATP1A1, blue staining is DAPI. Dashed yellow line – outlines sinusoids between hepatocytes. Green arrows point to the basal sides of hepatocytes, yellow asterixis depict cortical sides. Image representative of 2 animals. Scale bar, 10 μm.

Mapping nuclear and cytoplasmic mRNA distribution in multiple tissues

We next used our HiVis computational pipeline and spatial transcriptomics datasets to extract the relative distribution of mRNAs between the nucleus and cytoplasm. As a starting point, we analyzed the mouse liver (Fig. 6a), where nuclear retention of transcripts has been previously described using cell fractionation followed by RNA-seq (18). We identified transcripts enriched in either the cytoplasmic and nuclear compartments (Fig. 6b, Supplementary table 2). Cytoplasmic genes included the basally localized transcripts identified earlier, *Pigr* and *Scd1*, along with key hepatocyte markers such as *Apoc1*, *Apoa2*, *Apoe*, and *Alb*. Nuclear-enriched transcripts included *Mlxipl*, *Nlrp6*, *Sema4g* and *Pck1*. Correlation analysis revealed a strong positive agreement with the results of Bahar Halpern et al. (18) (r=0.66, p=3e-103, Fig. 6c), despite major differences in methodology, including bulk versus spatial resolution, poly(A) versus targeted capture, and overall sequencing strategies. Utilizing the ability to analyze zonal hepatocytes, we asked whether nuclear localization patterns vary across the liver lobule radial axis. We did not observe major differences in nuclear-cytoplasmic bias between central and portal regions, indicating that hepatocyte nuclear retention is consistent across the lobule (Fig. S5a). These findings validate that HiVis can reliably resolve nuclear-cytoplasmic mRNA distribution from VisiumHD data.

High-throughput mapping of nuclear–cytoplasmic mRNA localization has previously been explored in the mouse liver, yet not in the gastrointestinal tract nor in human. Therefore, we extended our analysis to additional tissues, including mouse proximal small intestine (Fig. 6d), human colon (Fig. 6e), as well as a recently published human liver dataset from a live organ donor (44) (Fig. 6f, S5b). While performed only in mouse liver, comparable analyses have not been carried out in these tissues. We used the H&E image to automatically extract the nuclear and cytoplasmic compartments. In each tissue, we detected transcripts preferentially localized to either the nuclear or cytoplasmic compartments (Fig. 6g-i, Supplementary table 2). We found that nuclear-cytoplasmic bias was conserved between mouse and human (Fig. S5c, r=0.71, p=1.7e-31), as well as between human liver and colon (Fig. S5d, r=0.74, p=1.3e-20). These findings establish HiVis as a versatile framework for characterizing nuclear-cytoplasmic mRNA localization in diverse tissue contexts.

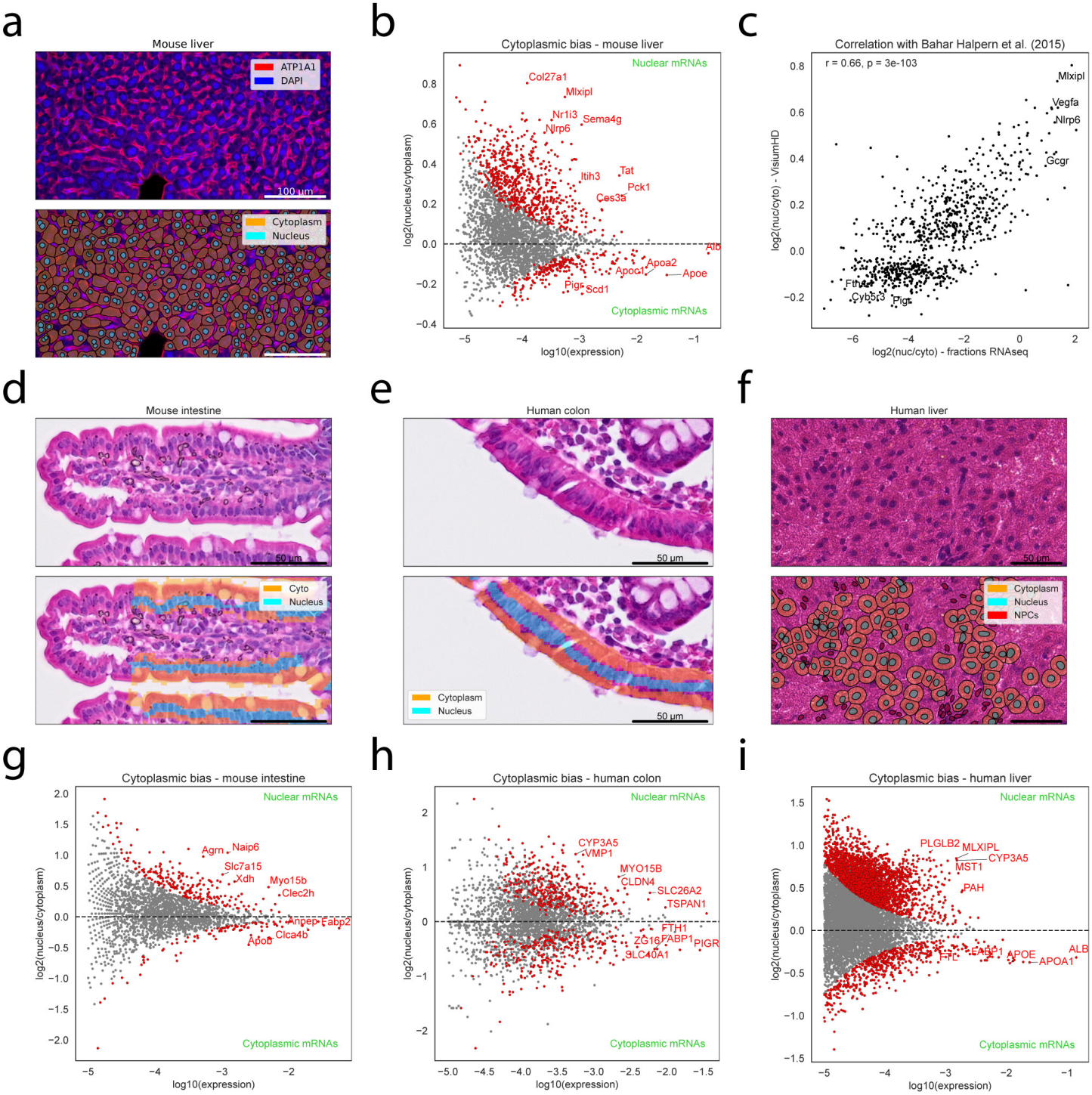

Figure 6 – Mapping nuclear retention across tissues

(a) Mouse liver VisiumHD immunofluorescence image (top) and overlayed with hepatocyte cellular and nuclear segmentation (bottom). **(b)** MA-plot of differential gene expression results in mouse liver. Significant genes (q<0.01) are colored red. Selected gene names are shown. **(c)** Spearman correlation plots of cytoplasmic/nuclear bias based on current VisiumHD and previously published RNA-seq (18). **(d, e, f)** Top – H&E images from VisiumHD of mouse proximal small intestine (d), human colon (e) and human liver (f). Bottom – same images as top, overlayed with 2×2µm bins colored by nuclear/cytoplasmic assignment. **(g, h, i)** MA-plot of differential gene expression results in mouse intestine (g), human colon (h) and human liver (i). Significant genes are colored red (g: q<0.05, h: q<0.25, i: q<0.05). Selected gene names are shown.

Discussion

mRNA localization is a widespread but incompletely understood phenomenon, particularly in epithelial cells (11). Although specific cases have been shown to be important for normal cell function (16), their extent across cell types and tissues remain unclear. With advances in high-resolution spatial transcriptomics, we set out to systematically map mRNA localization across tissues using the 10x VisiumHD platform. Applying this approach, we successfully characterized both apical-basal and nuclear-cytoplasmic biases in several tissues of the digestive system from mouse and human (Fig. 1). To enable these analyses, we developed HiVis, a flexible tool that streamlines analysis across diverse datasets by integrating image processing tools, tissue-specific single-cell segmentation, customized workflows, and subcellular transcript-localization analyses. In contrast to existing frameworks for subcellular transcriptomics, such as SPRAWL (28), Bento (29) and Ella (30), HiVis does not rely on isolated single-cell masks as the primary spatial unit. Instead, it integrates image-derived tissue context with segmentation outputs, allowing polarity features that depend on anatomical structure – such as lumen proximity in the intestine or sinusoidal orientation in the liver – to be captured. HiVis can also analyze binned spatial data when segmentation is incomplete, while still supporting full mask-based workflows when high-quality masks are available. Together, these features provide a unified framework for linking anatomical annotation, spatial zonation, and subcellular localization.

Our results showed strong concordance with previously published datasets, including LCM-derived profiles of apical and basal compartments from mouse intestinal epithelium and fractionated RNA-seq of nuclear and cytoplasmic compartments from mouse liver. Together, these comparisons support the accuracy of our approach for mapping global mRNA localization. Unlike the intestinal epithelium, the distinct morphology of hepatic plates complicates the characterization of apical–basal mRNA polarization in the liver. In this study, we combined membrane and endothelial staining with high-resolution spatial transcriptomics to identify, for the first time, a small set of hepatocyte transcripts exhibiting basal polarization. Our analyses further enabled comparison of mRNA localization across species and organs. Most localization patterns appeared conserved in both contexts. Moreover, although cells along tissue spatial axes – such as villi in the small intestine and lobules in the liver – show pronounced differences in expression levels, we observed little variation in mRNA localization across these zones. These findings suggest that under normal conditions, the subcellular localization of most mRNA species is largely preserved in epithelial cells of the digestive system. High-definition spatial transcriptomics has advanced rapidly in recent years, enabling increasingly detailed studies of gene expression within intact tissues. Although imaging-based approaches provide higher spatial resolution, they are often challenging to implement due to large data volumes, complex computational requirements, and most importantly – the limited number of targeted genes, which introduces bias. Sequencing-based spatial transcriptomics, in contrast, is highly scalable and continues to improve, though it remains constrained by molecular diffusion and spatial resolution. For example, the 2 μm resolution of VisiumHD can blur adjacent subcellular regions, causing perinuclear cytoplasmic transcripts to be misclassified as nuclear. Its major advantages include unbiased whole-transcriptome coverage and compatibility with FFPE samples, enabling exploratory analyses of archival and diseased tissues under diverse conditions. Building on these strengths, our approach adds a new layer of analysis that can reveal mRNA localization across tissues, cell types, and physiological or pathological contexts.

Methods

Experimental methods

Animal experiments and tissue preparations

Mouse experiments were approved by the Institutional Animal Care and Use Committee of the Weizmann Institute of Science (approval number 05220824–2) and performed in accordance with institutional guidelines. Two-months-old C57BL/6 male mice, housed under regular 12h light-dark cycle and fed ad libitum were used in the experiments. Mice were sacrificed by cervical dislocation and tissues were collected and fixed in 4% PFA in PBS in 4°C. Livers were incubated for 24 h, transferred to 70% Ethanol, embedded in paraffin, and stored at room temperature. Proximal jejunums were incubated for 3h, followed by overnight fixation in 4% FA + 30% sucrose at 4°C under gentle rotation. The jejunums were rolled to a "Swiss-rolls", embedded in OCT, and stored at −80°C.

Mouse liver VisiumHD experiment

VisiumHD spatial transcriptomics was performed on liver tissue sections from two male C57BL/6 mice (2.5 months old), following the official 10x Genomics protocol.

Immuno staining and fluorescence microscopy

Formalin-fixed, paraffin-embedded (FFPE) tissue blocks were sectioned into 5-µm slices and mounted onto poly-L-lysine-coated glass slides (Sigma-Aldrich, P0425).Tissue sections were immunostained according to the VisiumHD user guide. Primary antibodies included mouse anti-CD31 (ab28364, 1:100), rabbit anti-ATP1A1 (ab76020, 1:1000), and rabbit anti-LMNA (ab26300, 1:100), incubated for 90 minutes. Secondary antibodies were applied for 20 min, including donkey anti-mouse Cy3 (Jackson ImmunoResearch, 715-066-151, 1:200), donkey anti-rabbit Cy5 (Jackson ImmunoResearch, 711-175-152, 1:200), and DAPI (100 ng/mL, Sigma-Aldrich, D9542). Tissue sections were mounted in 85% glycerol in RNase-free water and covered with No. 1.5 coverslips (Marienfeld, 0102222). Fluorescence imaging was carried out on a widefield Leica DMi8 inverted microscope (Leica Microsystems Heidelberg GmbH, Germany) operated with LAS X software. The system was equipped with a Leica 12-bit monochrome camera (DFC7000GT-0127092118) and a multi-band fluorescence filter cube (QWF-S-T). Images were acquired with an HC PL APO 20×/0.80 dry objective (11506530) at a pixel size of 0.323 µm. A Tile Scan (XY mode) was performed using the LAS X Tile Scan function, and the resulting tiles were stitched in LAS X.

Library preparation and sequencing

Targeted transcript capture and amplification were carried out using the Mouse Probe Set v2 (10x Genomics). Ligated probes were transferred to VisiumHD spatial barcoding slides using CytAssist (v2.1.0.14) at 37 °C for 30 minutes, following the manufacturer's instructions. Library preparation was conducted using the VisiumHD Spatial Gene Expression User Guide, including 8 cycles of PCR for cDNA amplification. Prepared libraries from each slide were loaded onto individual lanes of an Illumina NovaSeq X flow cell at a concentration of 150 pM and sequenced.

Colon tissue collection and ethics declaration

Colon samples were obtained from patients undergoing colectomy for malignancy. All surgeries and FFPE block preparation were performed at Sheba Medical Center, Israel. This study was approved by the Sheba Medical Center Helsinki committee (approval number SMC-8665-21). All participants provided written informed consent prior to inclusion. The study was conducted in accordance with the Declaration of Helsinki and relevant local regulations

Single molecule fluorescence in situ hybridization

Mice Jejunums and livers were stained as previously described (55). Probe libraries were designed using the Stellaris FISH Probe Designer Software (Biosearch Technologies, Inc., Petaluma, California, United States of America). Probe libraries were coupled to Cy5, or Alexa 594. Cryosections (6 µm) of fixed mouse Jejunum or liver were mounted on poly-L-lysine pre-coated coverslips and used for probe hybridization. Sections were fixed for 15 min in 4% FA in PBS, washed with PBS, and incubated for 2 h in 70% ethanol in 4°C. Sections were washed with 2× SSC (Ambion AM9765) for 5 min, then permeabilized for 10 min with proteinase K (10 µg/ml, Ambion AM2546) followed by 2 washes with 2× SSC (Ambion AM9765) for 5 min. Tissues were incubated in wash buffer (Jejunum with 20%, livers with 15% Formamide Ambion AM9342, in 2× SSC) for 10 min in a 30°C incubator. Tissues were incubated with hybridization mix mixed with probes (Jejunum with 20%, livers with 15% Formamide, 10% Dextran sulfate Sigma D8906, 1 mg/ml *E. coli* tRNA Sigma R1753, 10% 20× SSC, 0.02% BSA Ambion AM2616, 2 mM Vanadylribonucleoside complex NEB S1402S, in Rnase-free water). For Jejunum sections – FITC-conjugated anti-CDH1 antibody (1:100, BD Biosciences cat. 612131) was added to hybridization mix, and for liver sections – anti-ATP1A1 antibody (1:1500, Abcam ab76020). Samples were incubated overnight in 30°C. After the hybridization, tissues were washed with wash buffer for 30 min in 30°C, and with wash buffer with DAPI (50 ng/ml, Sigma-Aldrich, D9542) for 10 min. Liver samples were incubated with Cy3 donkey anti-rabbit secondary antibody (1:200, Jackson Immuno Research, 711-165-152) together with DAPI for 20 min. Finally, tissues were washed twice with 2× SSC, and coverslips were mounted with ProLong Gold antifade reagent (Invitrogen P36934). Images were acquired using 100× magnification. All images were performed on a Nikon-Ti-E inverted fluorescence microscope using the NIS element software AR 5.02.03.

HCR-FISH

Colon samples were stained according to the Molecular Instruments HCR GOLD protocol for FFPE tissues. In brief, FFPE sections were deparaffinized and rehydrated through a graded ethanol series (Xylene, Xylene, 100% Ethanol, 100% Ethanol, 95% Ethanol, 70% Ethanol, 50% Ethanol, PBS). Sections were permeabilized for 10 min with 0.5% TritonX-100 (Sigma Aldrich) followed by two washes with PBS. Tissues were incubated in hybridization buffer (HiFi HCR hybridization buffer with 100 µg/ml salmon sperm DNA, Sigma-Aldrich D7656) for 10 min in a 37 °C incubator. Tissues were incubated with hybridization buffer mixed with probes (1:50) for 16 h in 37 °C. After the hybridization, tissues were washed with HiFi HCR wash 15 min in 37 °C for 4 times. The samples were incubated with amplification buffer (HCR amplification buffer with 100 µg/ml salmon sperm DNA) for 30 min at room temperature. HCR-hairpins (H1 and H2 hairpins of X1-

546, X3-647) were heated for 90 s at 95 °C and cooled in dark for 30 min. The samples were incubated with AB with 6 pmol of each hairpin for 60 min in the dark, and then rinsed twice in GOLD HCR wash buffer for 15 min. The samples were incubated with GOLD HCR wash buffer with DAPI (50 ng ml^{-1}, Sigma-Aldrich, D9542) for 5 min. Additional wash with GOLD HCR wash buffer was performed, and slides were mounted with Immu-Mount (Epredia, 990402). Images were acquired using 90× magnification.

All images were performed on a Nikon-Ti-E inverted fluorescence microscope using the NIS element software AR 5.02.03.

Computational methods

All analysis was performed using the HiVis tool (V0.9) in Python 3.10 and QuPath 0.6.0 (see code availability). Pixel classifiers in Qupath were trained using user-annotated examples for each class and relied solely on QuPath's built-in multiscale image features; No manually defined landmarks or distance-based features were used.

Mouse intestine

Publicly available VisiumHD mouse intestine dataset (C57BL/6 mouse, Cell Ranger v3.0, 10x Genomics, 2024, March 25) was imported, analyzed, and visualized in HiVis.

Single-cell segmentation and pixel classifiers

Single-cell segmentation was conducted in QuPath (35) using the Stardist extension (36) with the "he_heavy_augment" pretrained model and the following parameters:

- Threshold: 0.5
- Normalize Percentiles: 1, 99
- Cell expansion: 2 µm in muscle regions (defined by a pixel classifier) and 7 µm elsewhere.

Before nuclear expansion, areas without tissue (defined by a pixel classifier) were excluded, and nuclei identified as artefacts by an object classifier were removed.

Pixel classifiers were applied with the following settings:

- Classifier: Random trees
- Resolution: Moderate (2.19 µm/pixel)
- Features:
    - Channels: Hematoxylin, eosin
    - Scales: 1,2,4
    - All available features

Cell type annotations

Standard scRNA-seq analysis was performed with Scanpy (39). Genes expressed in fewer than 3 cells were removed. Data were normalized and log-transformed, and the 3000 most highly variable genes were

identified and retained. Gene expression values were scaled, and PCA was performed. A neighbors graph (n_neighbors=15) and Uniform Manifold Approximation and Projection (UMAP) (56) were computed on the first 30 PCs, and Leiden clustering was applied with a resolution of 0.5. Cell types were assigned to clusters based on known marker genes (Fig. S2c).

Villus zonation analysis

Epithelial-specific genes were defined using a signature matrix incorporating all major intestinal cell types, primarily based on Bahar et al. (57).Fibroblast markers were taken from Bahar et al. (58), and endothelial markers from Kalucka et al. (59):

$$Epithelial\ specific = \begin{cases} True & if\ \dfrac{E+pn}{N+pn} > 1 \\ False & Otherwise \end{cases}$$

Where *E* is the maximum expression in the Enterocytes and goblet cells, *N* is the maximum expression across all non-epithelial cell types, and *pn* the smallest non-zero value in *E*.

To quantify zonation along the villus axis, a pixel classifier was used to distinguish muscle from the remaining tissue. Individual villi were then manually segmented in QuPath. For each villus, the median coordinates of the muscle-associated bins were determined, and the distance of each bin from this reference point was calculated. Zonation bins were manually defined based on their distance from muscle:

- Base villus: 400–650 µm
- Mid villus: 650–900 µm
- Tip villus: ≥900 µm

Proximal small intestine, which had full undamaged villi was segmented manually in QuPath.

For correlation with previous tip/base scRNA-seq experiment (41), the published data was imported and tip and base were assigned as zones 1-2 and 5-6 respectively. In the VisiumHD data, tip and base identities were defined in cells from the epithelial cluster, in the proximal region. Spearman correlation was calculated on epithelial-specific genes with maximum normalized expression > 10^{-4} in both datasets.

Identification of basal, apical and nuclear genes

Apical, basal and nuclear identities were assigned to bins using a pixel classifier trained with the same parameters as above, except including scale 0.5. Apical and basal genes were also classified as cytoplasmic. Differential gene expressions between apical and basal, luminal-apical and perinuclear-apical, or nuclear and cytoplasmic bins was tested using Fisher's exact test. To avoid zonation bias, the analysis was restricted to the proximal intestine, limited to the base and mid villus zones, and focused on epithelial-specific genes. For correlation with previous apical/basal LCM experiment (14), data were imported, and Spearman correlation was calculated on genes with q-value < 0.25, mean normalized expression > 10^{-5} and $|\log_2(FC)| \geq 0.5$. For correlation of apical/basal bias between the tip and base of villi, the same test was applied to bins in these regions, and Spearman correlation was calculated on genes with q-value < 0.05 and mean normalized expression > 10^{-5}.

462 Quantification of smFISH intensity of apical genes

463 Luminal-apical and perinuclear-apical regions were manually segmented from epithelial cells located in
464 spatially distant villi from two mice, based on nuclear and membrane staining, using ImageJ (60). Mean
465 smFISH intensities for *Lct* and *Atp1b1* were quantified within each compartment, and background signal
466 was subtracted using measurements from adjacent non-cellular regions. The ratio of luminal-to-
467 perinuclear background-subtracted intensities was then calculated for each cell, and statistical
468 significance was assessed using a Wilcoxon signed-rank test.

469

470 Human colon

471 Published VisiumHD data of human colon (25) were imported, analyzed, and visualized in HiVis. Only
472 adjacent-normal or control tissues were included in the analysis.

473 Epithelial-specific genes were defined using a signature matrix obtained from Dan et al. (61).

474
$$Epithelial\ specific = \begin{cases} True & if\ \frac{E+pn}{N+pn} > 1\ \ and\ E > 1 * 10^{-5} \\ & False\ \ Otherwise \end{cases}$$

475 Where *E* is the maximum expression in the enterocytes and goblet cells, *N* is the mean expression across
476 all non-epithelial cell types, and *pn* is the smallest non-zero value in *E*.

477 Apical, basal and nuclear identities were assigned to bins by manual annotation in QuPath (35). Apical and
478 basal genes were also classified as cytoplasmic. Differential gene expression analysis was performed on
479 epithel-specific genes, excluding mitochondrial genes. Fisher's exact test was conducted for each sample
480 individually. To integrate results across samples, for each gene $\log_2$FC was taken as the median across all
481 samples, expression level as the mean, and one-sided p-values were combined using Fisher's method
482 (62). One-sided p-values were concatenated, and corrected for multiple hypothesis testing using the
483 Benjamini-Hochberg method (63), after which they assigned back as one-sided q-values.

484 For correlation with a previous apical/basal LCM dataset of human small intestine (14), data were
485 imported, and Spearman correlation was calculated on genes with q-value < 0.25.

486

487 Mouse liver

488 Raw FASTQ files generated by the sequencer were processed using Space Ranger (v3.1.2, 10x Genomics),
489 including manual image alignment, spatial barcoding, read alignment to the mm10 reference genome, and
490 UMI counting. VisiumHD data from mouse livers were imported, analyzed, and visualized using HiVis.
491 Since the VisiumHD slides contained additional samples from unrelated projects, both the expression
492 data and corresponding images were cropped to the liver regions, and pixels from other samples were
493 excluded. Correlation of expression levels between the two liver samples was assessed using Spearman's
494 correlation.

Single cell segmentation

Single-cell segmentation was performed in QuPath (35) using the Cellpose (37,64) and StarDist (36) extensions. The whole tissue was first segmented using a Random trees pixel classifier, keeping only regions larger than 25 μm^2, and closing holes smaller than 50 μm^2. A second pixel classifier was applied to identify the blood vessel regions. Hepatocytes were segmented within the whole tissue mask, using a custom-trained Cellpose model with both ATP1A1 and DAPI channels, and were allowed to expand into blood vessel regions to allow smooth segmentation. The model was trained to delineate the exact borders of hepatocytes, enabling accurate segmentation of mononuclear, binuclear, and cells without nucleus in the imaging plane. Training was performed on 100 regions (120 × 120 µm each) sampled from the dataset. Segmentation performance was evaluated by selecting an additional 20 regions (10 from each sample) and manually segmenting ~80 cells per region, defined as a ground truth (GT) dataset. Our applied custom Cellpose model was compared against the built-in cyto3 Cellpose model – both based on membrane and nuclei signals – and against nuclei segmentation with expansion approach using Stardist and Cellpose (Supplementary Table 3). To assess segmentation performance an intersection-over-union (IoU) was computed for each pair of matching cells. IoU was computed as the number of intersecting pixels between the two segmented objects divided by the union of the pixels of the two objects. A correct match was considered only if IoU was larger than 0.5, namely if the overlap between the GT and the segmented cell encompassed more than 50% of the pixels in the union of both objects. Following this calculation, commonly used precision metrics were computed, including recall, F1 score Aggregated Jaccard Index (AJI):

$$Object\ F1 = \frac{2 \cdot TP}{2 \cdot TP + FP + FN}$$

$$Average\ precision = \frac{TP}{TP + FP + FN}$$

$$Object\ precision = \frac{TP}{TP + FP}$$

$$Object\ recall = \frac{TP}{TP + FN}$$

$$Aggregated\ Jaccard\ Index\ (AJI) = \frac{\sum |\ GT_i \cap Pred_j\ |}{\sum |\ GT_i \cap Pred_j\ | + unmatched\ areas}$$

Where TP denotes true positive detections, defined as one-to-one matches between ground truth (GT) objects, and predictions with an IoU ≥ 0.5. FP denotes false positive detections (predicted objects not matched to any GT object), and FN denotes false negatives (GT objects without a corresponding prediction). AJI computes the sum over all matched pairs of their overlapping pixels divided by this sum and the total sum of areas that are unmatched (both non-overlapping pixels in matched pairs and total pixels of unmatched objects and GT).

To allow analyses based on nuclear counts, nuclei were segmented independently using the built-in *cyto3* model, and each nucleus was subsequently matched to its parent cell. NPCs were segmented within blood vessel regions using an in-house–trained StarDist model on the DAPI channel (65), with expansion restricted to vessel regions and capped at 2 µm. The StarDist threshold was set to 0.3 with normalization

percentiles of 1 and 99. NPC were further filtered by size (nuclear area 10-80 μm^2) and by DAPI intensity >18,000.

Lobule zonation analysis

Hepatocyte zonation was inferred using previously published periportal and pericentral marker gene lists (46) by calculating the zonation score $\eta = \frac{PP}{PP+PC}$, where PP is the sum of the normalized expression of periportal markers and PC is the sum of normalized expression of pericentral markers. The zonation score was binned into six groups using the Fisher-Jenks method (66), and zones were smoothed by calculating the median within a 40 μm radius kernel.

Comparison of gene zonation between samples and with previously published data (47,50) was performed using a center-of-mass (COM) calculation for each gene g:

$$COM_g = \frac{\sum_z (E_{g,z} \cdot z)}{E_{g,z}}$$

Where $E_{g,z}$ is the expression level of gene g in zone z, and z is the numeric index of the zone (ranging from 1 to 6). When comparing VisiumHD with the other datasets, the average expression per zone was computed over the pooled cells from both VisiumHD samples prior to COM calculation. The resulting COM values were correlated using Spearman's correlation.

Zonal ploidy probabilities

To determine the probability of hepatocyte ploidy states across zones, nuclear areas were quantified separately for mononucleated and binucleated hepatocytes in each lobular zone. In binucleated cells, the summed areas of both nuclei were considered. For each group, nuclear area distributions were binned into 50 histogram intervals and smoothed (kernel size = 3 bins). Local maxima were detected, and the minimum between the two maxima was used as the decision boundary between diploid and tetraploid nuclei. Mononuclear hepatocytes with nuclear areas below or above this threshold were assigned as 2n or 4n respectively, whereas bi-nucleated hepatocytes with nuclear areas below or above this threshold were assigned as 2n+2n or 4n+4n respectively.

Within each mouse and zone, the proportion of hepatocytes in each ploidy state was calculated as the number of cells in that ploidy class divided by the total number of hepatocytes of the same nuclearity class. These per-mouse proportions were then averaged across mice for each zone and ploidy state.

Identification of basal, cortical and nuclear genes

To find large blood vessels and sinusoids between hepatocytes, a pixel classifier was applied with the following parameters:

- Classifier: Random trees
- Resolution: Moderate (2.57 μm/pixel)
- Features:
    - Channels: CD31, ATP1A1, DAPI, autofluorescence
    - Scales: 0.5, 1, 2, 4
    - All available features

The distance from each bin center to the nearest sinusoid pixel was computed. Bin identities were then assigned as follows:

- Blood vessel: Bins with >90% coverage by blood vessel identity
- Basal: bins within 1.5 μm of a blood vessel
- Apical: non-basal bins within 1.5 μm of the cell border
- Cytoplasmic: all remaining non-apical, non-basal bins outside the nucleus

Hepatocyte-specific genes were defined using a signature matrix incorporating all major liver cell types based on Ben-Moshe et al. (67):

$$Hepatocyte\ specific = \begin{cases} True & if\ \frac{E+pn}{N+pn} > 1\ \ and\ E > 1 * 10^{-5} \\ & False\ \ Otherwise \end{cases}$$

Where *E* is the expression in hepatocytes, *N* is the average expression across all non-hepatocyte cell types, and *pn* the smallest non-zero value in *E*.

Differential gene expression analysis was performed on cells with >500 UMIs, restricted to hepatocyte-specific genes, excluding mitochondrial genes. For basal/cortical analysis, only cells with at least three basal bins and with <20% coverage classified as "blood vessel", (by the pixel classifier), were included. Fisher's exact test was applied on each sample individually. To combine both samples, for each gene the $\log_2$FC and expression level were averaged across samples, and one-sided p-values were combined using Fisher's method (62). One-sided p-values were concatenated, and corrected for multiple hypothesis testing using the Benjamini-Hochberg method (63), after which they assigned back as one-sided q-values.

For correlation with previously published nuclear/cytoplasmic fraction RNA-seq data (18), the data were imported and processed by averaging the two nuclear and two cytoplasmic replicates separately. A $\log_2$(nuclear/cytoplasmic) expression ratio was then computed. Spearman correlation was performed using genes with mean normalized expression $>10^{-4}$ in both datasets and q-value <0.25. To compute the correlation between nuclear to cytoplasmic ratio between central and portal regions, the same test was applied in both zones (central: zones 1,2; portal: zones 5,6), and Spearman's correlation was calculated on the genes with q-value <0.25 and max normalized expression $>10^{-5}$.

Human liver

Published data and single-hepatocyte segmentation (44) were imported and analyzed in HiVis. Only one sample (M6), which showed high RNA capture rates, was used in the analysis. Hepatocytes zonation was computed as previously described (44) by calculating the zonation score $\eta = \frac{PP}{PP+PC}$, where PP is the summed expression of periportal markers, and PC is the summed expression of pericentral markers. The zonation score was binned into four groups using the Fisher-Jenks method (66), and zones were smoothed by calculating the median within a 50μm radius kernel. Differential gene expression analysis between nuclear and cytoplasmic bins was performed using Fisher's exact test, restricted to bins in zones 2,3.

Data availability

The VisiumHD datasets analyzed in this study originate from a combination of publicly available and internal sources. Mouse intestine dataset is available for download from the 10x Genomics website (https://www.10xgenomics.com/datasets). The human liver dataset was obtained from Yakubovsky et al. (44), and the human colon dataset from Oliveira et al., 2025 (25). The mouse liver dataset is available in [ZENODO link will be available upon publication].

Code availability

HiVis is available as a Python package via PyPI distribution at https://pypi.org/project/HiVis/. The source code for the HiVis package and the QuPath scripts, together with usage examples, is available in the HiVis GitHub repository: https://github.com/roynov01/HiVis. Detailed documentation is provided at https://hivis.readthedocs.io/latest/. The code used for the analyses in this study is available in [GITHUB link will be available upon publication] and has also been deposited in Zenodo under accession [ZENODO link will be available upon publication].

Author's contributions

R.N and S.I conceived the study. R.N and O.G conceived the HiVis tool and performed image analysis. R.N developed the Python code and wrote the documentation. O.G developed the Groovy code. R.N and M.K performed the VisiumHD experiment on mouse liver. T.B and I.G contributed to fluorescence image acquisition. I.K performed the surgeries. I.K, M.F and I.N provided colon samples. S.I supervised the project. R.N and S.I wrote the manuscript. All authors contributed to the manuscript revisions and approved the final version.

Acknowledgments

We thank Ron Moran for assistance with packaging our tool for distribution via pip. We thank Jacob Elkahal and Eldad Tzahor for providing the CD31 antibody. We thank Elizabeth Vaisbourd for the insightful feedback that improved the clarity and presentation of the figures. S.I. is supported by the Helen and Martin Kimmel Award for Innovative Investigation, the Yad Abraham Research Center for Cancer Diagnostics and Therapy, the Moross Integrated Cancer Center, a Weizmann-Sheba grant, the Israel Science Foundation grants no. 908/21 and 3663/21, the European Research Council (ERC) under the European Union's Horizon 2020 research and innovation programme grant no. 768956 and a grant from the Ministry of Innovation, Science & Technology, Israel. Optical imaging acquired at the de Picciotto Cancer Cell Observatory In memory of Wolfgang and Ruth Lesser of the Moross Integrated Cancer Center in the department of Life Science Core Facilities, Weizmann Institute of Science.

Supplementary tables

Supplementary table 1 – Zonation analysis results.

Supplementary table 2 – Subcellular compartments DGE analysis results.

Supplementary table 3 – Segmentation evaluation results.

Supplementary figures

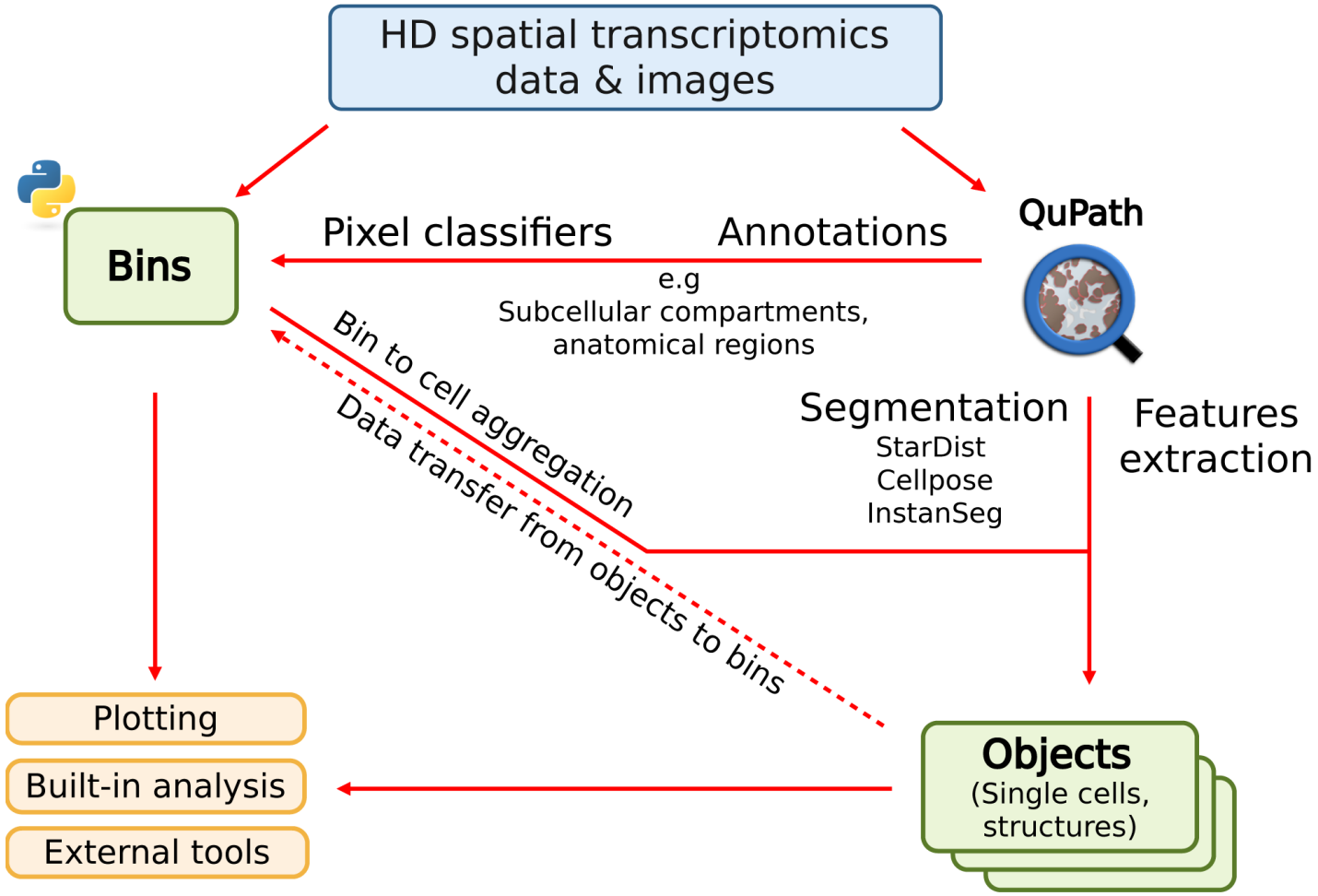

Figure S1 – Diagram of the HiVis tool

HiVis is a user-friendly platform for high-definition spatial transcriptomics analysis. Image analysis is performed with QuPath, whereas all other steps are implemented in Python, including aggregation of bins into cells or other objects. HiVis operates at both the bin and aggregation levels, synchronizing data across them. It provides flexible, fully customizable plotting, offers built-in analysis methods, and is compatible with external tools such as Scanpy (39) and Squidpy (40). The diagram was created with BioRender.com.

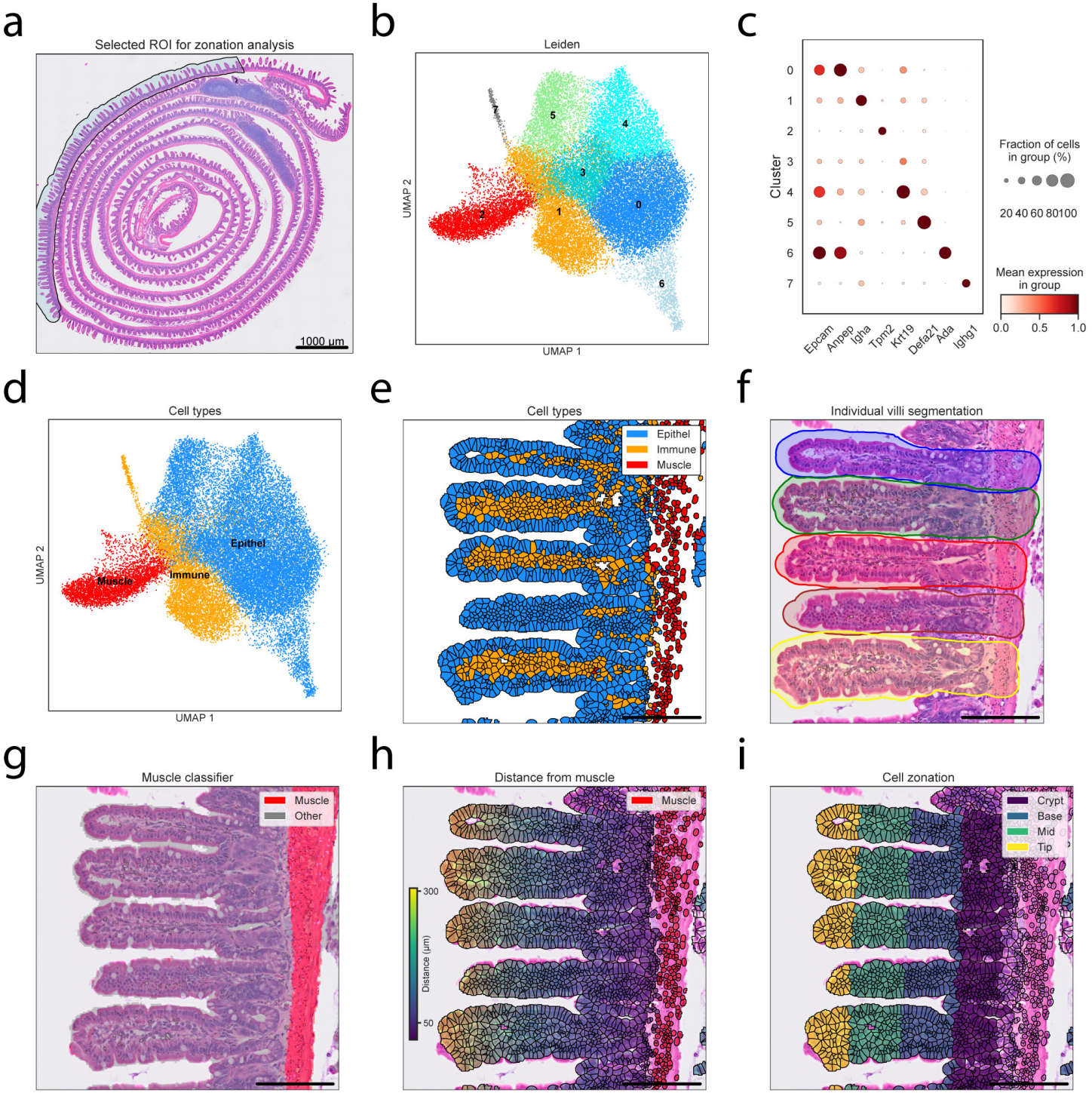

Figure S2 – Reconstructing zonation along villi in mouse small intestine

(a) VisiumHD H&E image of mouse small intestine, overlayed with proximal intestine annotation for further analysis. (b) UMAP of single cells colored by leiden clusters. **(c)** Dot plot of normalized gene expression for selected markers across leiden clusters. **(d)** Annotated UMAP of single cells colored by cell type. **(e)** Cells colored by cell type. **(f)** VisiumHD H&E image of mouse proximal intestine, overlayed with individual villi manual annotations. **(g)** Mouse proximal intestine VisiumHD H&E image overlayed with 2×2µm bins colored by muscle identity, based on a pixel classifier. **(h)** Mouse proximal intestine VisiumHD H&E image overlayed with cells colored by the distance from the muscle layer. **(i)** Mouse proximal intestine VisiumHD H&E image overlayed with cells colored by the villus zone. Scale bar in (e-i) – 100µm.

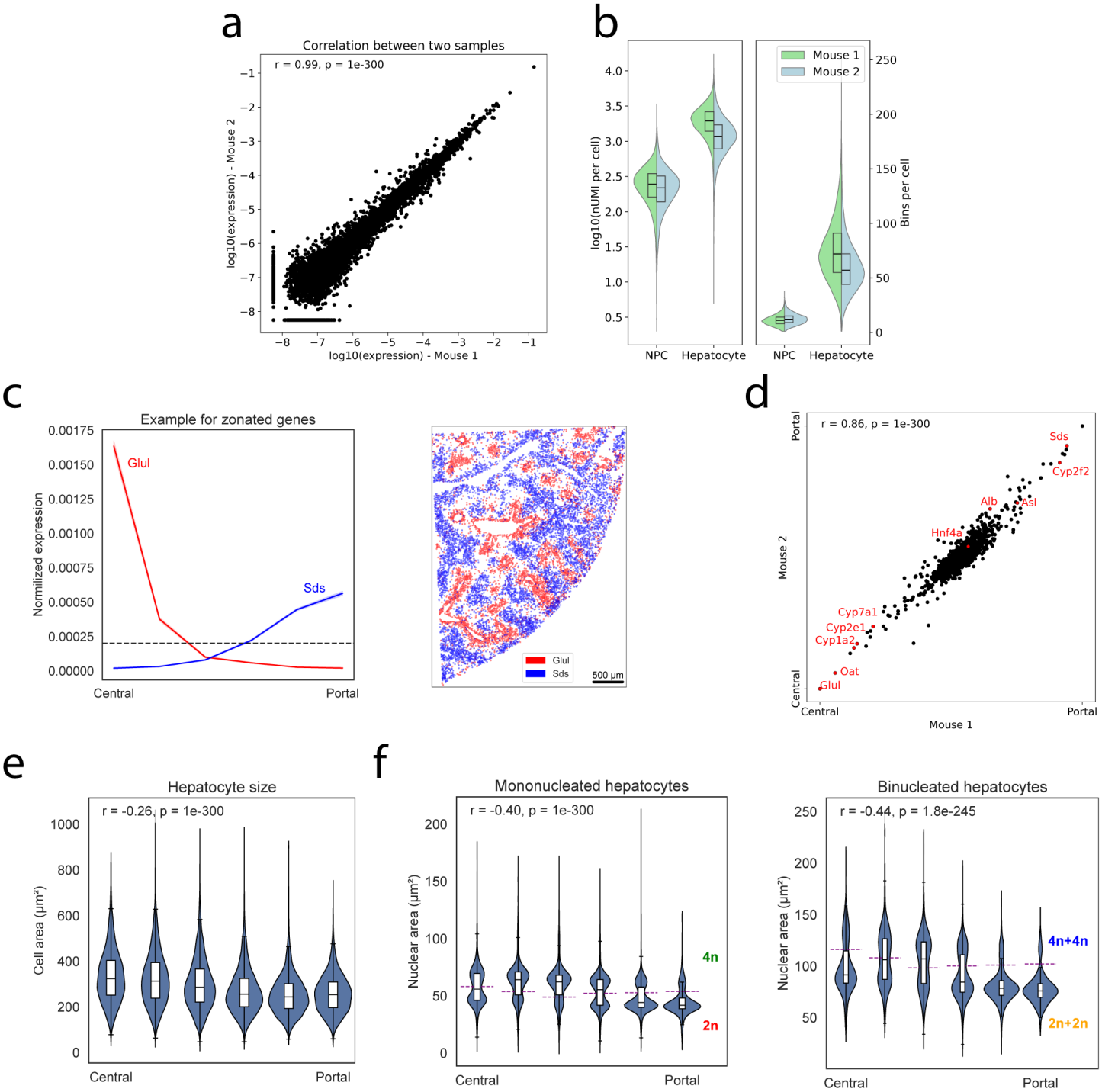

Figure S3 – Reconstructing hepatocyte zonation across liver lobules

(a) Spearman correlation of normalized gene expression levels between both mice in the experiment. **(b)** Distribution of nUMI (left) and number of 2×2 µm bins (right) in cells from two VisiumHD mouse liver samples. NPC – non parenchymal cells. **(c)** Examples of two zonated genes in single-cell data from mouse liver VisiumHD. Left – normalized expression across liver lobules, data is mean expression, and patch is standard error of the mean. Right – spatial plot of single cells colored by expression of each of the genes. Cells are colored if above the normalized expression > 0.0002. **(d)** Spearman correlation plots of center of mass across liver zones from the two mice in the experiment. **(e)** Violin plots with boxplots showing cell areas of hepatocytes across liver zones. Data is from two samples. Correlation is spearman. **(f)** Violin plots with boxplots showing nuclear area of hepatocytes across liver zones for mononucleated (left) and binucleated (right) hepatocytes. The purple dashed lines mark thresholds

separating ploidy classes, indicated by colored labels. Data is from two samples. Correlation is spearman. In boxplots (b, e-f) – horizontal bars are medians, boxes delineate the 25–75 percentiles.

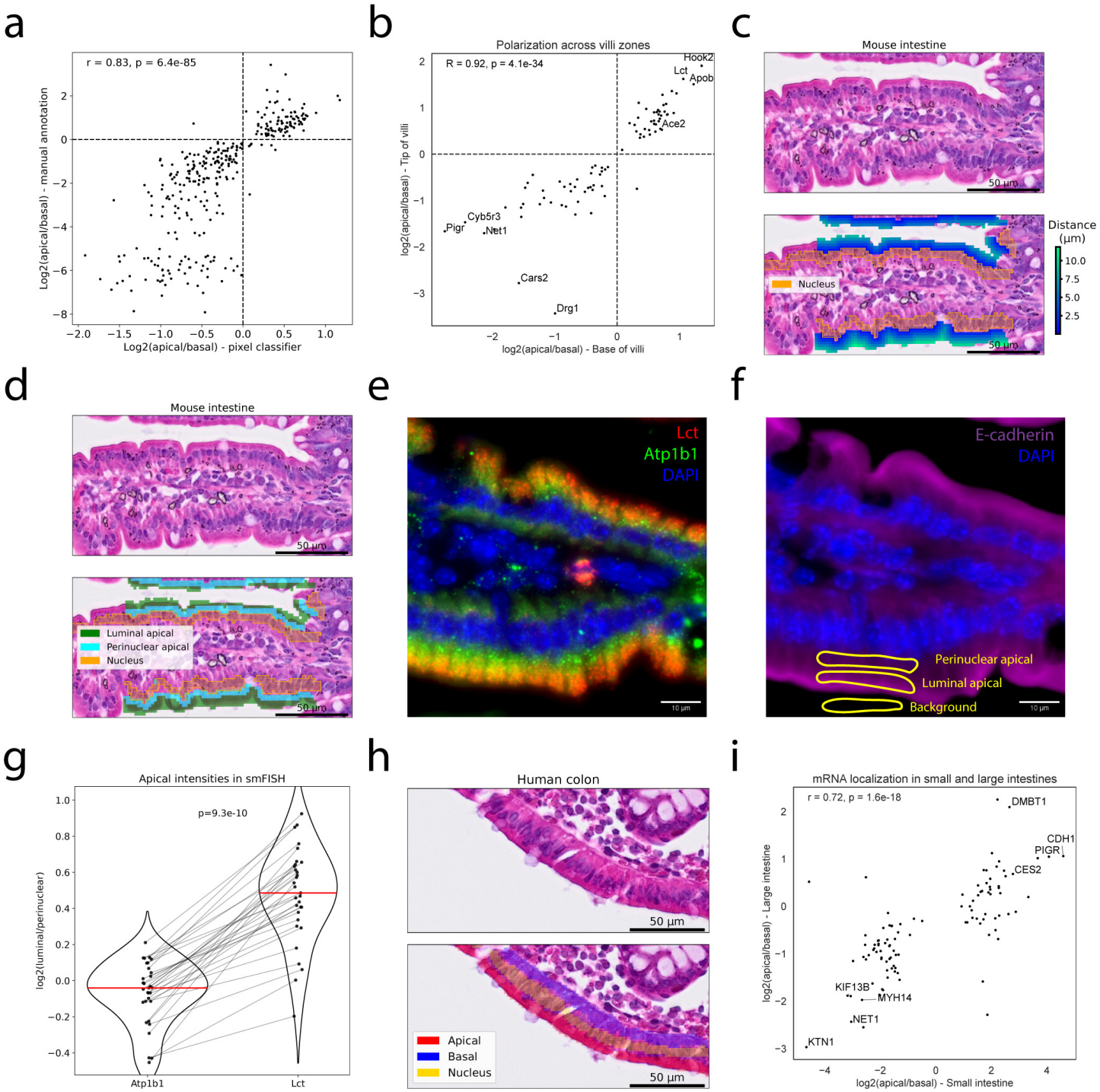

Figure S4 – Mapping apical-basal polarization in mouse small intestine and human colon

(a) Spearman correlation of apical-basal bias in mouse proximal intestine using manual annotation and pixel classifier. *Genes with normalized expression > 10^{-5} and q<0.05 are used*. **(b)** Spearman correlation of apical-basal bias in base and tip of villi in mouse proximal intestine. Only genes with q<0.05 and normalized expression > 10^{-5} in both zones are used. Selected gene names are shown. **(c)** Mouse proximal intestine VisiumHD H&E image (top) and overlayed with 2×2µm bins colored by the distance to the nuclei (bottom). **(d)** Mouse proximal intestine VisiumHD H&E image (top) and overlayed with 2×2µm bins colored by apical sub-compartments (bottom). **(e)** smFISH staining of Lct and Atp1b1 in mouse proximal intestine. Image is representative of 2 mice. Scale bar, 10 µm. **(f)** Example

annotation of apical sub-compartments and background, used for quantification of smFISH intensity. Annotations are based on Immunofluorescence staining of E-cadherin and nuclei. Same FOV as (e). **(g)** Quantification of apical smFISH signal as log2(luminal/perinuclear) intensity for Atp1b1 and Lct. Lines connect paired measurements across annotated apical sub-compartments. Red lines indicate medians. p-value calculated by Wilcoxon signed-rank test. Annotations are from two mice. **(h)** Human colon VisiumHD H&E image (top) and overlayed with 2×2µm bins colored by apical/basal assignment (bottom). **(i)** Spearman correlation of apical-basal bias in colon and Jejunum. Jejunum data is based on previously published LCM RNA-seq (14). Only genes with q<0.25 in both datasets are used. Selected gene names are shown.

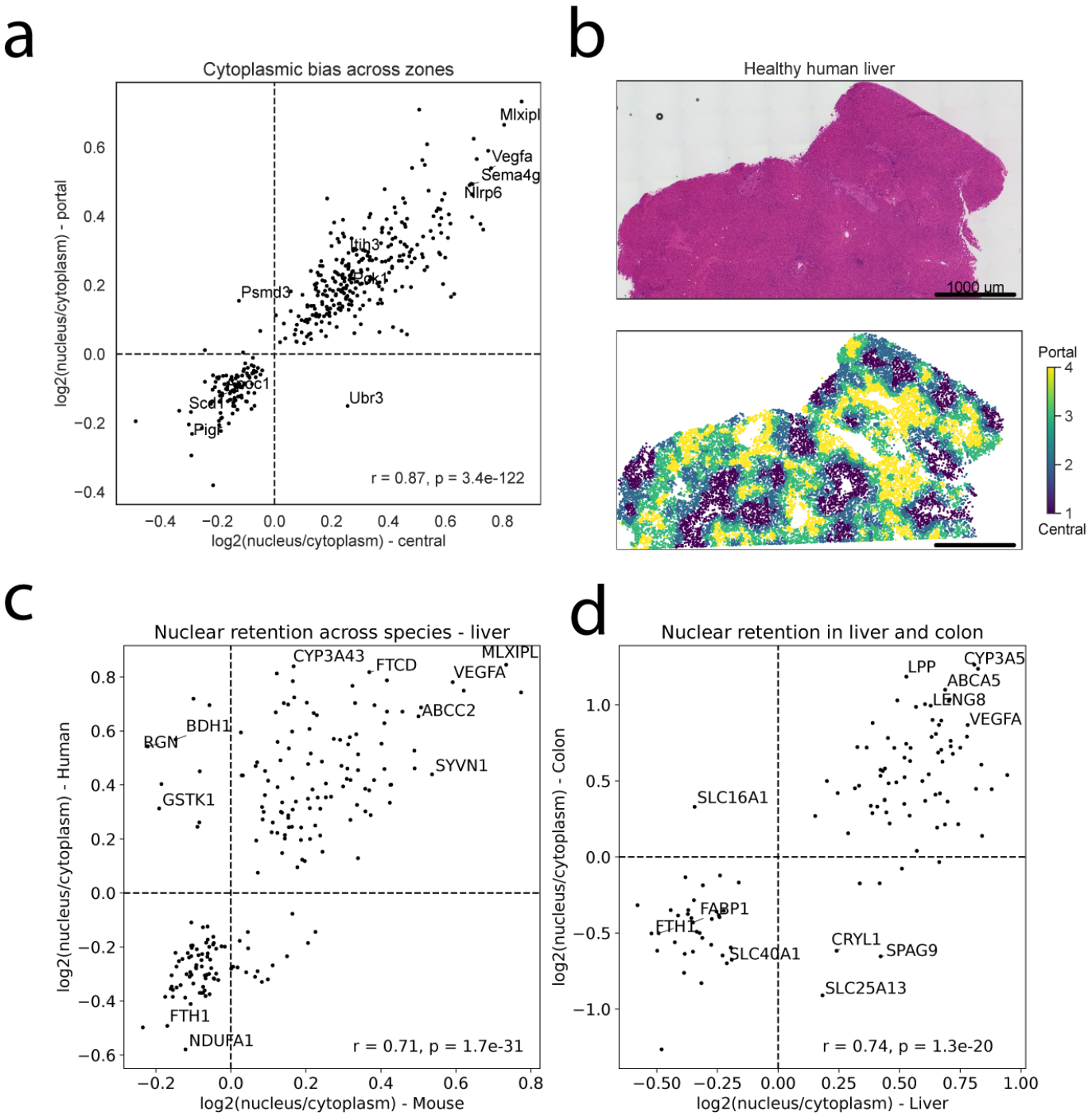

Figure S5 – Mapping nuclear retention in livers

(a) Spearman correlation of nuclear/cytoplasmic bias in pericentral and periportal mouse liver zones. Only genes with q<0.05 and normalized expression > 10^{-4} in both zones are used. Selected gene names are shown. **(b)** Top –

human liver VisiumHD H&E image. Bottom – single-cell VisiumHD data of human liver, colored by zones along the central-portal axis. **(c)** Spearman correlation of nuclear/cytoplasmic bias in human and mouse livers. Only genes with $q<0.05$ and normalized expression > 10^{-4} in both species are used. Selected gene names are shown. **(d)** Spearman correlation of nuclear/cytoplasmic bias in human colon and liver. Only genes with $q<0.05$ and normalized expression > 10^{-4} in both organs are used. Selected gene names are shown.

References

1. Engel KL, Arora A, Goering R, Lo HYG, Taliaferro JM. Mechanisms and consequences of subcellular RNA localization across diverse cell types. Traffic. 2020;21(6):404–18.

2. Hawdon A, Geoghegan ND, Mohenska M, Elsenhans A, Ferguson C, Polo JM, et al. Apicobasal RNA asymmetries regulate cell fate in the early mouse embryo. Nat Commun. 2023 May 30;14(1):2909.

3. Liao G, Mingle L, Van De Water L, Liu G. Control of Cell Migration Through Mrna Localization and Local Translation. Wiley Interdiscip Rev RNA. 2015 Jan;6(1):1–15.

4. Buxbaum AR, Haimovich G, Singer RH. In the right place at the right time: visualizing and understanding mRNA localization. Nat Rev Mol Cell Biol. 2015 Feb;16(2):95–109.

5. Das S, Vera M, Gandin V, Singer RH, Tutucci E. Intracellular mRNA transport and localized translation. Nat Rev Mol Cell Biol. 2021 July;22(7):483–504.

6. Mili S, Moissoglu K, Macara IG. Genome-wide screen reveals APC-associated RNAs enriched in cell protrusions. Nature. 2008 May;453(7191):115–9.

7. Martin KC, Ephrussi A. mRNA Localization: Gene Expression in the Spatial Dimension. Cell. 2009 Feb 20;136(4):719–30.

8. Cajigas IJ, Tushev G, Will TJ, tom Dieck S, Fuerst N, Schuman EM. The Local Transcriptome in the Synaptic Neuropil Revealed by Deep Sequencing and High-Resolution Imaging. Neuron. 2012 May 10;74(3):453–66.

9. Poon MM, Choi SH, Jamieson CAM, Geschwind DH, Martin KC. Identification of Process-Localized mRNAs from Cultured Rodent Hippocampal Neurons. J Neurosci. 2006 Dec 20;26(51):13390–9.

10. Buxbaum AR, Yoon YJ, Singer RH, Park HY. Single-molecule insights into mRNA dynamics in neurons. Trends Cell Biol. 2015 Aug 1;25(8):468–75.

11. Wang J, Horlacher M, Cheng L, Winther O. RNA trafficking and subcellular localization—a review of mechanisms, experimental and predictive methodologies. Brief Bioinform. 2023 Sept 1;24(5):bbad249.

12. Barth JA, Li W, Krasinski SD, Montgomery RK, Verhave M, Grand RJ. Asymmetrical Localization of mRNAs in Enterocytes of Human Jejunum. J Histochem Cytochem. 1998 Mar 1;46(3):335–43.

13. Moor AE, Golan M, Massasa EE, Lemze D, Weizman T, Shenhav R, et al. Global mRNA polarization regulates translation efficiency in the intestinal epithelium. Science. 2017 Sept 22;357(6357):1299–303.

14. Novoselsky R, Harnik Y, Yakubovsky O, Katina C, Levin Y, Halpern KB, et al. Intracellular polarization of RNAs and proteins in the human small intestinal epithelium. PLOS Biol. 2024 Dec 2;22(12):e3002942.

15. Goering R, Arora A, Pockalny MC, Taliaferro JM. RNA localization mechanisms transcend cell morphology. Singer RH, Manley JL, Chao J, editors. eLife. 2023 Mar 3;12:e80040.

16. Mason DE, Madsen TD, Gasparski AN, Kong D, Jiwnani N, Lechler T, et al. Control of epithelial tissue organization by mRNA localization. Nat Commun. 2025 June 5;16(1):5216.

17. Wegener M, Müller-McNicoll M. Nuclear retention of mRNAs - quality control, gene regulation and human disease. Semin Cell Dev Biol. 2018 July;79:131–42.

18. Bahar Halpern K, Caspi I, Lemze D, Levy M, Landen S, Elinav E, et al. Nuclear Retention of mRNA in Mammalian Tissues. Cell Rep. 2015 Dec 29;13(12):2653–62.

19. Liu Y, Beyer A, Aebersold R. On the Dependency of Cellular Protein Levels on mRNA Abundance. Cell. 2016 Apr 21;165(3):535–50.

20. Battich N, Stoeger T, Pelkmans L. Control of Transcript Variability in Single Mammalian Cells. Cell. 2015 Dec 17;163(7):1596–610.

21. Janesick A, Shelansky R, Gottscho AD, Wagner F, Williams SR, Rouault M, et al. High resolution mapping of the tumor microenvironment using integrated single-cell, spatial and in situ analysis. Nat Commun. 2023 Dec 19;14(1):8353.

22. Chen KH, Boettiger AN, Moffitt JR, Wang S, Zhuang X. Spatially resolved, highly multiplexed RNA profiling in single cells. Science. 2015 Apr 24;348(6233):aaa6090.

23. He S, Bhatt R, Brown C, Brown EA, Buhr DL, Chantranuvatana K, et al. High-plex Multiomic Analysis in FFPE at Subcellular Level by Spatial Molecular Imaging [Internet]. bioRxiv; 2022 [cited 2025 Sept 3]. p. 2021.11.03.467020. Available from: https://www.biorxiv.org/content/10.1101/2021.11.03.467020v3

24. Eng CHL, Lawson M, Zhu Q, Dries R, Koulena N, Takei Y, et al. Transcriptome-scale super-resolved imaging in tissues by RNA seqFISH+. Nature. 2019 Apr;568(7751):235–9.

25. Oliveira MF de, Romero JP, Chung M, Williams SR, Gottscho AD, Gupta A, et al. High-definition spatial transcriptomic profiling of immune cell populations in colorectal cancer. Nat Genet. 2025 June;57(6):1512–23.

26. Chen A, Liao S, Cheng M, Ma K, Wu L, Lai Y, et al. Spatiotemporal transcriptomic atlas of mouse organogenesis using DNA nanoball-patterned arrays. Cell. 2022 May 12;185(10):1777-1792.e21.

27. Rodriques SG, Stickels RR, Goeva A, Martin CA, Murray E, Vanderburg CR, et al. Slide-seq: A scalable technology for measuring genome-wide expression at high spatial resolution. Science. 2019 Mar 29;363(6434):1463–7.

28. Bierman R, Dave JM, Greif DM, Salzman J. Statistical analysis supports pervasive RNA subcellular localization and alternative 3' UTR regulation. Wagner EJ, Weigel D, editors. eLife. 2024 Dec 19;12:RP87517.

29. Mah CK, Ahmed N, Lopez NA, Lam DC, Pong A, Monell A, et al. Bento: a toolkit for subcellular analysis of spatial transcriptomics data. Genome Biol. 2024 Apr 2;25(1):82.

30. Wang JX, Zhou X. ELLA: Modeling Subcellular Spatial Variation of Gene Expression within Cells in High-Resolution Spatial Transcriptomics [Internet]. bioRxiv; 2024 [cited 2025 Nov 4]. p. 2024.09.23.614515. Available from: https://www.biorxiv.org/content/10.1101/2024.09.23.614515v1

31. Polański K, Bartolomé-Casado R, Sarropoulos I, Xu C, England N, Jahnsen FL, et al. Bin2cell reconstructs cells from high resolution Visium HD data. Bioinformatics. 2024 Sept 1;40(9):btae546.

32. Marconato L, Palla G, Yamauchi KA, Virshup I, Heidari E, Treis T, et al. SpatialData: an open and universal data framework for spatial omics. Nat Methods. 2025 Jan;22(1):58–62.

33. Kamel M, Song Y, Solbas A, Villordo S, Sarangi A, Senin P, et al. ENACT: End-to-End Analysis of Visium High Definition (HD) Data. Bioinformatics. 2025 Mar 1;41(3):btaf094.

34. Zhang P, Chen W, Tran TN, Zhou M, Carter KN, Kandel I, et al. Thor: a platform for cell-level investigation of spatial transcriptomics and histology. Nat Commun. 2025 Aug 5;16(1):7178.

35. Bankhead P, Loughrey MB, Fernández JA, Dombrowski Y, McArt DG, Dunne PD, et al. QuPath: Open source software for digital pathology image analysis. Sci Rep. 2017 Dec 4;7(1):16878.

36. Weigert M, Schmidt U. Nuclei instance segmentation and classification in histopathology images with StarDist [Internet]. 2022 [cited 2024 Aug 21]. Available from: http://arxiv.org/abs/2203.02284

37. Stringer C, Wang T, Michaelos M, Pachitariu M. Cellpose: a generalist algorithm for cellular segmentation. Nat Methods. 2021 Jan;18(1):100–6.

38. Goldsborough T, Philps B, O'Callaghan A, Inglis F, Leplat L, Filby A, et al. InstanSeg: an embedding-based instance segmentation algorithm optimized for accurate, efficient and portable cell segmentation [Internet]. arXiv; 2024 [cited 2025 Sept 1]. Available from: http://arxiv.org/abs/2408.15954

39. Wolf FA, Angerer P, Theis FJ. SCANPY: large-scale single-cell gene expression data analysis. Genome Biol. 2018 Feb 6;19:15.

40. Palla G, Spitzer H, Klein M, Fischer D, Schaar AC, Kuemmerle LB, et al. Squidpy: a scalable framework for spatial omics analysis. Nat Methods. 2022 Feb;19(2):171–8.

41. Moor AE, Harnik Y, Ben-Moshe S, Massasa EE, Rozenberg M, Eilam R, et al. Spatial Reconstruction of Single Enterocytes Uncovers Broad Zonation along the Intestinal Villus Axis. Cell. 2018 Nov 1;175(4):1156-1167.e15.

42. Harnik Y, Yakubovsky O, Hoefflin R, Novoselsky R, Bahar Halpern K, Barkai T, et al. A spatial expression atlas of the adult human proximal small intestine. Nature. 2024 Aug;632(8027):1101–9.

43. Halpern KB, Shenhav R, Matcovitch-Natan O, Tóth B, Lemze D, Golan M, et al. Single-cell spatial reconstruction reveals global division of labour in the mammalian liver. Nature. 2017 Feb;542(7641):352–6.

44. Yakubovsky O, Afriat A, Egozi A, Halpern KB, Barkai T, Harnik Y, et al. A spatial transcriptomics atlas of live donors reveals unique zonation patterns in the healthy human liver [Internet]. bioRxiv; 2025 [cited 2025 Aug 31]. p. 2025.02.22.639181. Available from: https://www.biorxiv.org/content/10.1101/2025.02.22.639181v1

45. Zwick RK, Kasparek P, Palikuqi B, Viragova S, Weichselbaum L, McGinnis CS, et al. Epithelial zonation along the mouse and human small intestine defines five discrete metabolic domains. Nat Cell Biol. 2024 Feb;26(2):250–62.

46. Droin C, Kholtei JE, Bahar Halpern K, Hurni C, Rozenberg M, Muvkadi S, et al. Space-time logic of liver gene expression at sub-lobular scale. Nat Metab. 2021 Jan;3(1):43–58.

47. Xu J, Guo P, Hao S, Shangguan S, Shi Q, Volpe G, et al. A spatiotemporal atlas of mouse liver homeostasis and regeneration. Nat Genet. 2024 May;56(5):953–69.

48. Morales-Navarrete H, Segovia-Miranda F, Klukowski P, Meyer K, Nonaka H, Marsico G, et al. A versatile pipeline for the multi-scale digital reconstruction and quantitative analysis of 3D tissue architecture. Watt FM, editor. eLife. 2015 Dec 17;4:e11214.

49. Tanami S, Ben-Moshe S, Elkayam A, Mayo A, Bahar Halpern K, Itzkovitz S. Dynamic zonation of liver polyploidy. Cell Tissue Res. 2017 May 1;368(2):405–10.

50. Halpern KB, Shenhav R, Matcovitch-Natan O, Tóth B, Lemze D, Golan M, et al. Single-cell spatial reconstruction reveals global division of labour in the mammalian liver. Nature. 2017 Feb;542(7641):352–6.

51. Massey-Harroche D. Epithelial cell polarity as reflected in enterocytes. Microsc Res Tech. 2000 May 15;49(4):353–62.

52. Buckley CE, St Johnston D. Apical–basal polarity and the control of epithelial form and function. Nat Rev Mol Cell Biol. 2022 Aug;23(8):559–77.

53. Thottacherry JJ, Chen J, Johnston DS. Apical-basal polarity in the gut. Semin Cell Dev Biol. 2023 Dec 1;150–151:15–22.

54. Ben-Moshe S, Itzkovitz S. Spatial heterogeneity in the mammalian liver. Nat Rev Gastroenterol Hepatol. 2019 July;16(7):395–410.

55. Lyubimova A, Itzkovitz S, Junker JP, Fan ZP, Wu X, van Oudenaarden A. Single-molecule mRNA detection and counting in mammalian tissue. Nat Protoc. 2013 Sept;8(9):1743–58.

56. McInnes L, Healy J, Melville J. UMAP: Uniform Manifold Approximation and Projection for Dimension Reduction [Internet]. arXiv; 2020 [cited 2025 Sept 3]. Available from: http://arxiv.org/abs/1802.03426

57. Bahar Halpern K, Korem Kohanim Y, Biram A, Harnik Y, Egozi A, Yakubovsky O, et al. The cellular states and fates of shed intestinal cells. Nat Metab. 2023 Nov;5(11):1858–69.

58. Bahar Halpern K, Massalha H, Zwick RK, Moor AE, Castillo-Azofeifa D, Rozenberg M, et al. Lgr5+ telocytes are a signaling source at the intestinal villus tip. Nat Commun. 2020 Apr 22;11(1):1936.

59. Kalucka J, de Rooij LPMH, Goveia J, Rohlenova K, Dumas SJ, Meta E, et al. Single-Cell Transcriptome Atlas of Murine Endothelial Cells. Cell. 2020 Feb 20;180(4):764-779.e20.

60. Schindelin J, Arganda-Carreras I, Frise E, Kaynig V, Longair M, Pietzsch T, et al. Fiji: an open-source platform for biological-image analysis. Nat Methods. 2012 July;9(7):676–82.

61. Dan S, Ungar B, Ben-Moshe S, Halpern KB, Yavzori M, Fudim E, et al. Distal Fecal Wash Host Transcriptomics Identifies Inflammation Throughout the Colon and Terminal Ileum. Cell Mol Gastroenterol Hepatol. 2023 Jan 1;16(1):1–15.

62. Fisher RA. Statistical Methods for Research Workers. In: Kotz S, Johnson NL, editors. Breakthroughs in Statistics: Methodology and Distribution [Internet]. New York, NY: Springer; 1992 [cited 2025 Aug 31]. p. 66–70. Available from: https://doi.org/10.1007/978-1-4612-4380-9_6

63. Benjamini Y, Hochberg Y. Controlling the False Discovery Rate: A Practical and Powerful Approach to Multiple Testing. J R Stat Soc Ser B Methodol. 1995;57(1):289–300.

64. Burri O, Sobolewski P, Fehlmann T. BIOP/qupath-extension-cellpose: Improved label image reading and code linting [Internet]. Zenodo; 2024 [cited 2025 Mar 21]. Available from: https://zenodo.org/records/13752036

65. Mardamshina M, Karagach S, Mohan V, Arad G, Necula D, Golani O, et al. Integrated spatial proteomic analysis of breast cancer heterogeneity unravels cancer cell phenotypic plasticity. Nat Commun. 2025 Nov 25;16(1):10482.

66. F. Jenks G. The Data Model Concept in Statistical Mapping, International Yearbook of Cartography 7. 1967. 186–190 p.

67. Ben-Moshe S, Veg T, Manco R, Dan S, Papinutti D, Lifshitz A, et al. The spatiotemporal program of zonal liver regeneration following acute injury. Cell Stem Cell. 2022 June 2;29(6):973-989.e10.

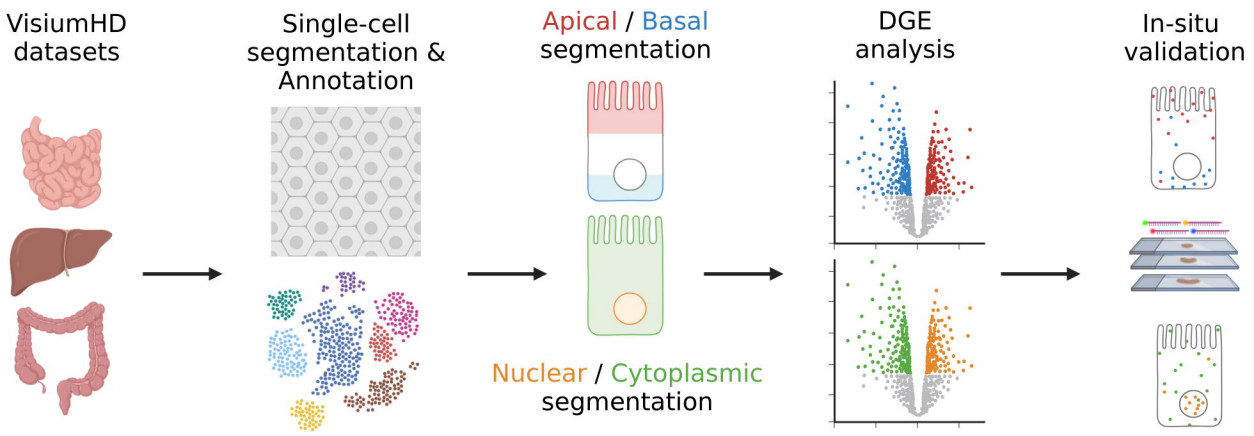
VisiumHD datasets
Single-cell segmentation & Annotation
Apical / Basal segmentation
Nuclear / Cytoplasmic segmentation
DGE analysis
In-situ validation

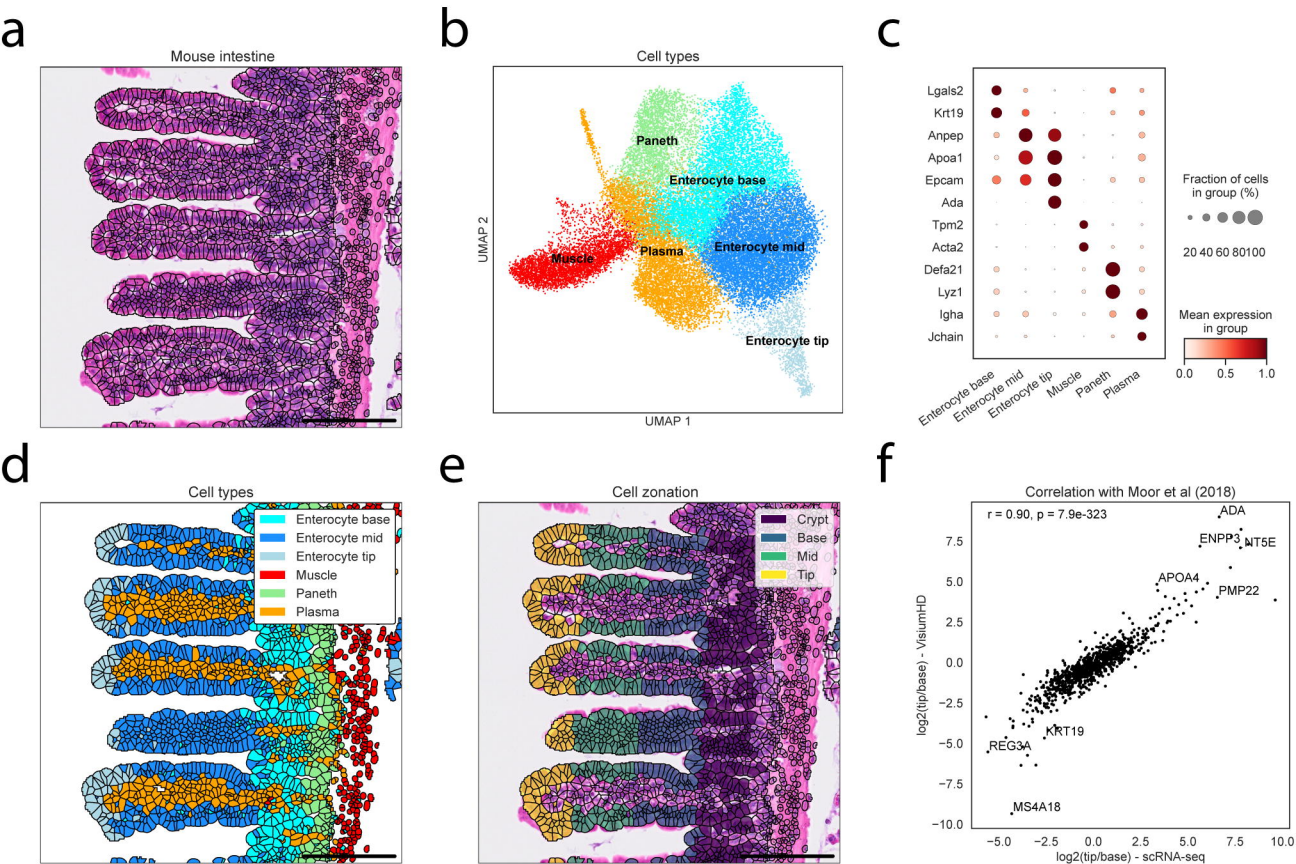
a
Mouse intestine
b
Cell types
Paneth
Enterocyte base
Muscle
Plasma
Enterocyte mid
Enterocyte tip
UMAP 2
UMAP 1
c
Lgals2
Krt19
Anpep
Apoa1
Epcam
Ada
Tpm2
Acta2
Defa21
Lyz1
Igha
Jchain
Enterocyte base
Enterocyte mid
Enterocyte tip
Muscle
Paneth
Plasma
Fraction of cells in group (%)
20 40 60 80100
Mean expression in group
0.0 0.5 1.0
d
Cell types
Enterocyte base
Enterocyte mid
Enterocyte tip
Muscle
Paneth
Plasma
e
Cell zonation
Crypt
Base
Mid
Tip
f
Correlation with Moor et al (2018)
r = 0.90, p = 7.9e-323
ADA
ENPP3
NT5E
APOA4
PMP22
KRT19
REG3A
MS4A18
log2(tip/base) - VisiumHD
log2(tip/base) - scRNA-seq

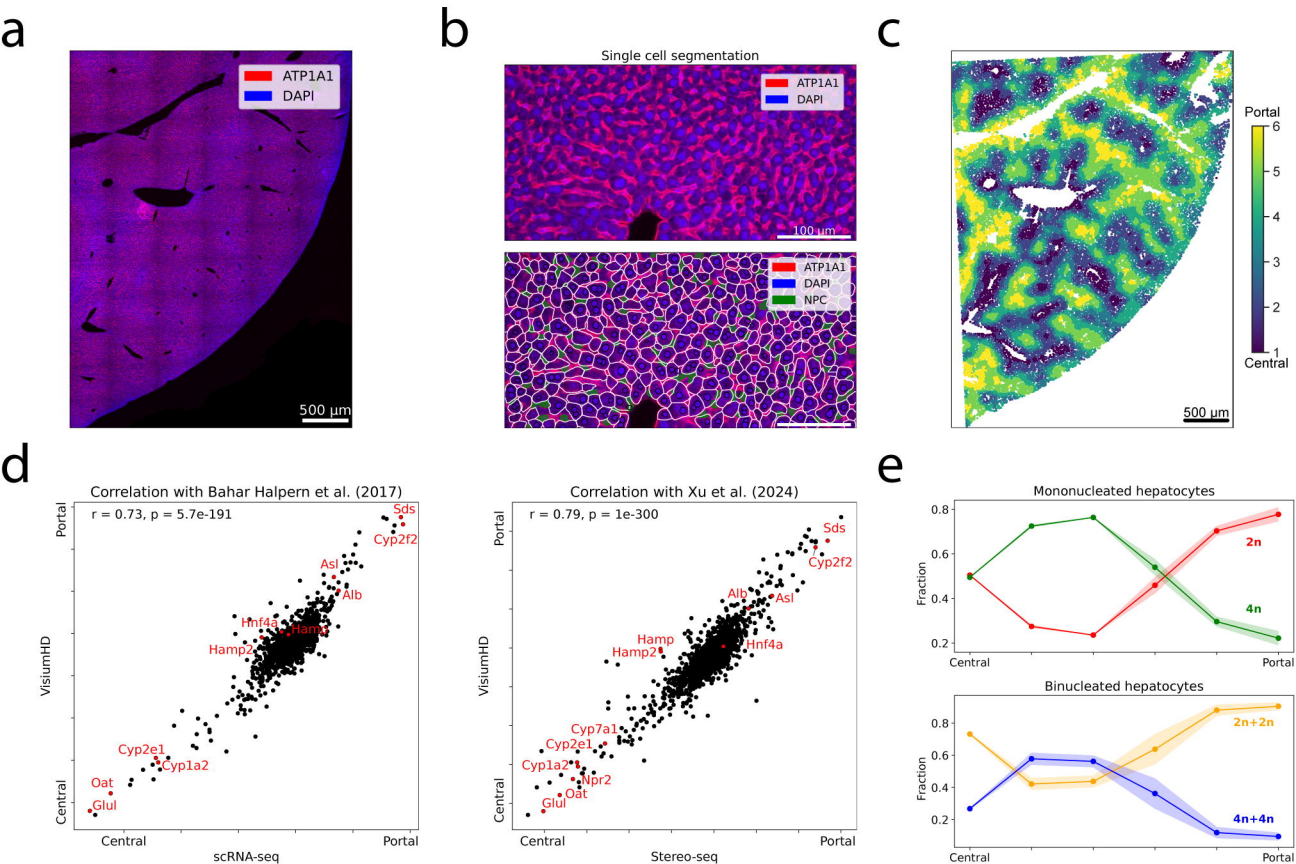
a
ATP1A1
DAPI
500 µm
b
Single cell segmentation
ATP1A1
DAPI
100 µm
ATP1A1
DAPI
NPC
c
Portal
6
5
4
3
2
1
Central
500 µm
d
Correlation with Bahar Halpern et al. (2017)
r = 0.73, p = 5.7e-191
Portal
VisiumHD
Central
Central
Portal
scRNA-seq
Sds
Cyp2f2
Asl
Alb
Hnf4a
Hamp
Hamp2
Cyp2e1
Cyp1a2
Oat
Glul
Correlation with Xu et al. (2024)
r = 0.79, p = 1e-300
Portal
VisiumHD
Central
Central
Portal
Stereo-seq
Sds
Cyp2f2
Alb
Asl
Hamp
Hamp2
Hnf4a
Cyp7a1
Cyp2e1
Cyp1a2
Npr2
Oat
Glul
e
Mononucleated hepatocytes
Fraction
0.8
0.6
0.4
0.2
2n
4n
Central
Portal
Binucleated hepatocytes
Fraction
0.8
0.6
0.4
0.2
2n+2n
4n+4n
Central
Portal

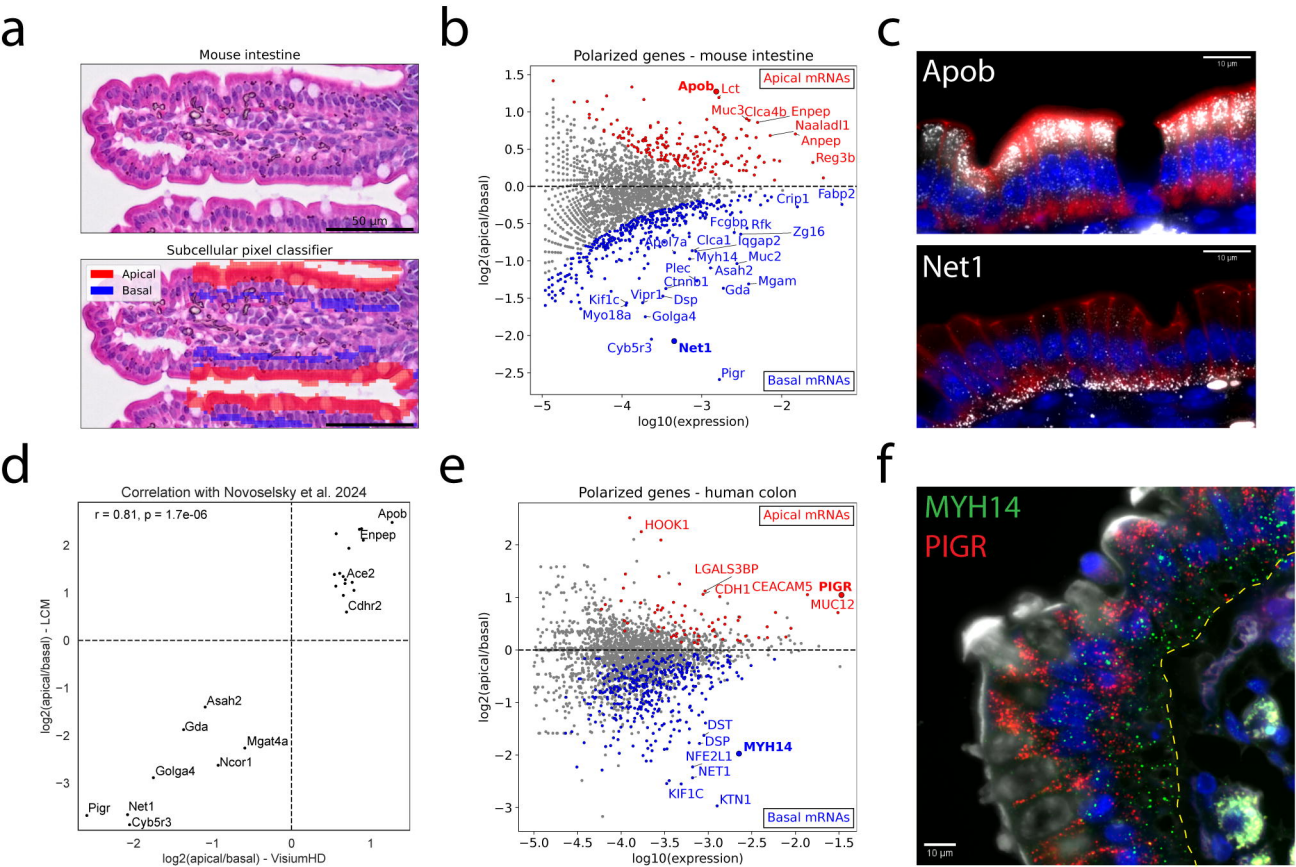
a
Mouse intestine
50 µm
Subcellular pixel classifier
Apical
Basal
b
Polarized genes - mouse intestine
Apical mRNAs
Basal mRNAs
Apob
Lct
Muc3
Clca4b
Enpep
Naaladl1
Anpep
Reg3b
Fabp2
Crip1
Fcgbp
Rfk
Zg16
Clca1
Iqgap2
Anol7a
Myh14
Muc2
Plec
Asah2
Ctnnb1
Mgam
Gda
Kif1c
Vipr1
Dsp
Myo18a
Golga4
Cyb5r3
Net1
Pigr
log2(apical/basal)
log10(expression)
c
Apob
Net1
10 µm
d
Correlation with Novoselsky et al. 2024
r = 0.81, p = 1.7e-06
Apob
Enpep
Ace2
Cdhr2
Asah2
Gda
Mgat4a
Ncor1
Golga4
Pigr
Net1
Cyb5r3
log2(apical/basal) - LCM
log2(apical/basal) - VisiumHD
e
Polarized genes - human colon
Apical mRNAs
Basal mRNAs
HOOK1
LGALS3BP
CDH1
CEACAM5
PIGR
MUC12
DST
DSP
MYH14
NFE2L1
NET1
KIF1C
KTN1
log2(apical/basal)
log10(expression)
f
MYH14
PIGR
10 µm

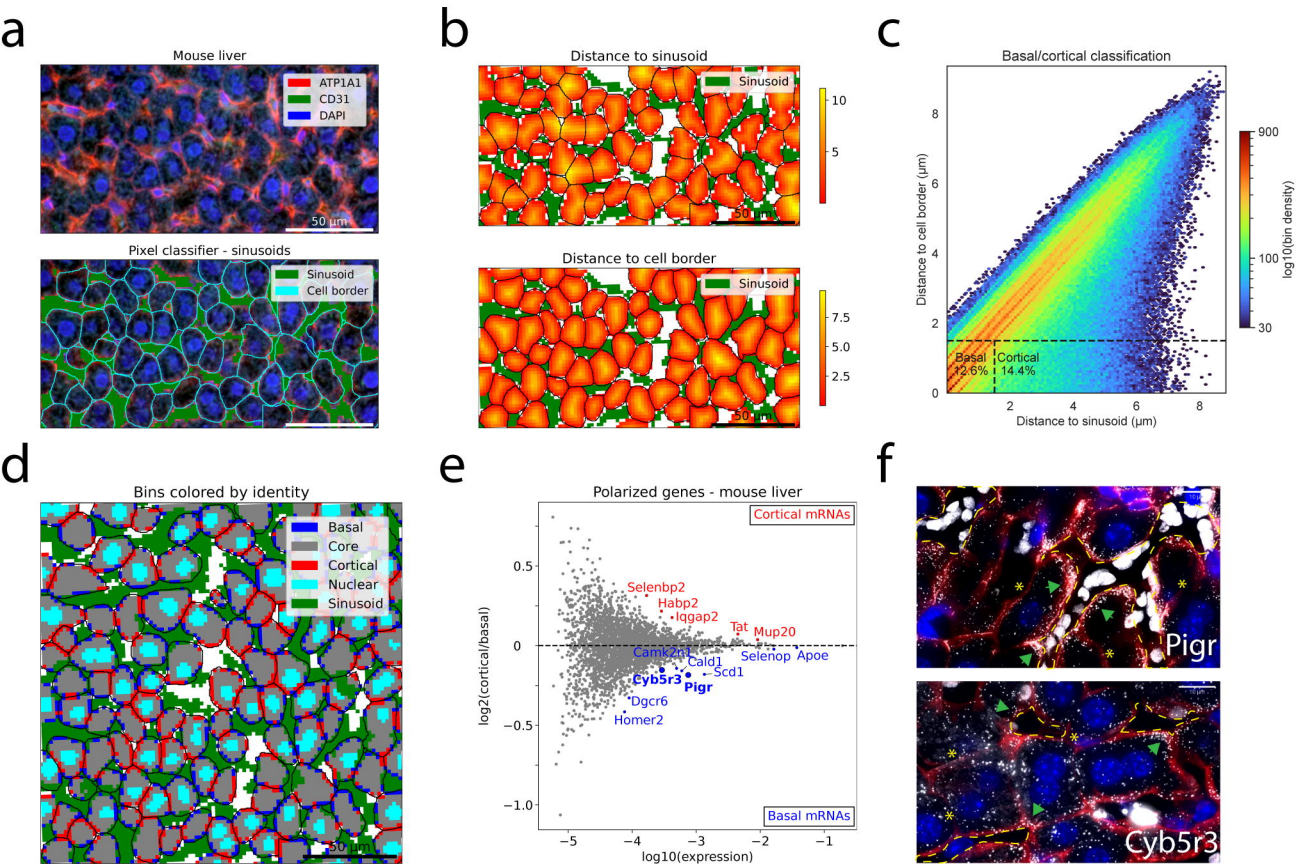
a
Mouse liver
ATP1A1
CD31
DAPI
50 µm
Pixel classifier - sinusoids
Sinusoid
Cell border
b
Distance to sinusoid
Sinusoid
10
5
50 µm
Distance to cell border
Sinusoid
7.5
5.0
2.5
50 µm
c
Basal/cortical classification
Distance to cell border (µm)
Distance to sinusoid (µm)
log10(bin density)
900
100
30
Basal
12.6%
Cortical
14.4%
d
Bins colored by identity
Basal
Core
Cortical
Nuclear
Sinusoid
50 µm
e
Polarized genes - mouse liver
Cortical mRNAs
Basal mRNAs
log2(cortical/basal)
log10(expression)
Selenbp2
Habp2
Iqgap2
Tat
Mup20
Selenop
Apoe
Camk2n1
Cald1
Scd1
Cyb5r3
Pigr
Dgcr6
Homer2
f
Pigr
Cyb5r3

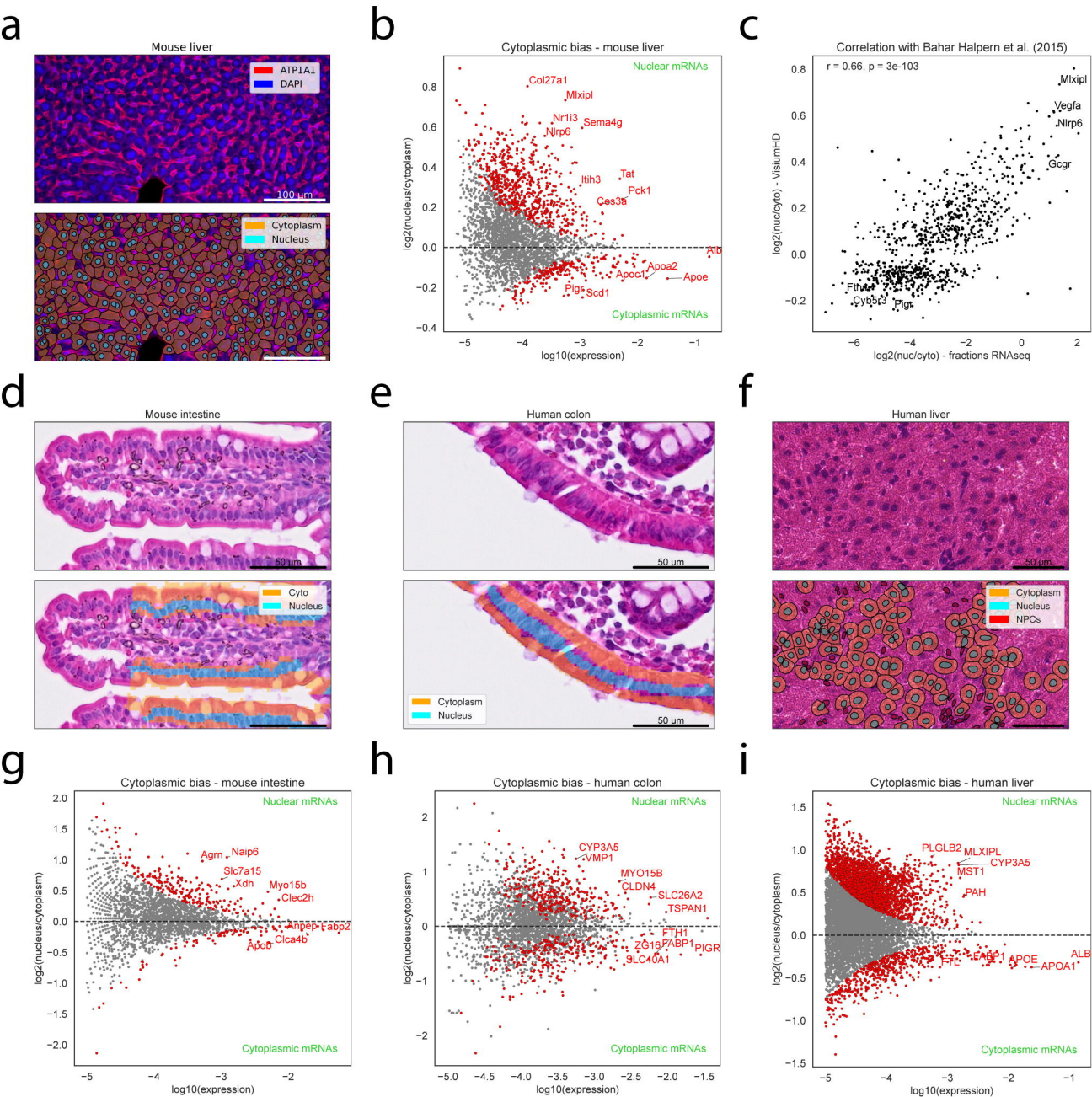
a
Mouse liver
ATP1A1
DAPI
100 µm
Cytoplasm
Nucleus
b
Cytoplasmic bias - mouse liver
Nuclear mRNAs
Cytoplasmic mRNAs
Col27a1
Mlxipl
Nr1i3
Sema4g
Nlrp6
Itih3
Tat
Pck1
Ces3a
Alb
Apoa2
Apoc1
Apoe
Pigr
Scd1
log2(nucleus/cytoplasm)
log10(expression)
c
Correlation with Bahar Halpern et al. (2015)
r = 0.66, p = 3e-103
Mlxipl
Vegfa
Nlrp6
Gcgr
Fthl17
Cyb5r3
Pigr
log2(nuc/cyto) - VisiumHD
log2(nuc/cyto) - fractions RNAseq
d
Mouse intestine
50 µm
Cyto
Nucleus
e
Human colon
50 µm
Cytoplasm
Nucleus
f
Human liver
50 µm
Cytoplasm
Nucleus
NPCs
g
Cytoplasmic bias - mouse intestine
Nuclear mRNAs
Cytoplasmic mRNAs
Agrn
Naip6
Slc7a15
Xdh
Myo15b
Clec2h
Anpep
Fabp2
Clca4b
Apob
log2(nucleus/cytoplasm)
log10(expression)
h
Cytoplasmic bias - human colon
Nuclear mRNAs
Cytoplasmic mRNAs
CYP3A5
VMP1
MYO15B
CLDN4
SLC26A2
TSPAN1
FTH1
ZG16
FABP1
PIGR
SLC40A1
log2(nucleus/cytoplasm)
log10(expression)
i
Cytoplasmic bias - human liver
Nuclear mRNAs
Cytoplasmic mRNAs
PLGLB2
MLXIPL
CYP3A5
MST1
PAH
APOE
APOA1
ALB
log2(nucleus/cytoplasm)
log10(expression)